The Astrophysical Journal, 670:15–38, 2007 November 20
© 2007. The American Astronomical Society. All rights reserved. Printed in U.S.A.

THE SIGHTLINE TO Q2343–BX415: CLUES TO GALAXY FORMATION IN A QUASAR ENVIRONMENT[1]

Samantha A. Rix,[2] Max Pettini,[3] Charles C. Steidel,[4] Naveen A. Reddy,[5]
Kurt L. Adelberger,[6] Dawn K. Erb,[7] and Alice E. Shapley[8]

Received 2007 February 22; accepted 2007 July 23

ABSTRACT

We have discovered a strong DLA coincident in redshift with the faint QSO Q2343–BX415 ($\mathcal{R} = 20.2$, $z_{em} = 2.57393$). Follow-up observations at intermediate spectral resolution reveal that the metal lines associated with this proximate DLA (PDLA) consist of two sets of absorption components. One set is moving toward the quasar with velocities of $\sim$150–600 km s^{-1}; this gas is highly ionized and does not fully cover the continuum source, suggesting that it is physically close to the active nucleus. The other, which accounts for most of the neutral gas, is blueshifted relative to the QSO, with the strongest component at ~ -160 km s^{-1}. We consider the possibility that the PDLA arises in the outflowing interstellar medium of the host galaxy of Q2343–BX415, an interpretation supported by strong C IV and N V absorption at nearby velocities, and by the intense radiation field longward of the Lyman limit implied by the high C II*/H I ratio. If Q2343–BX415 is the main source of these UV photons, then the PDLA is located at either $\sim$8 or $\sim$37 kpc from the active nucleus. Alternatively, the absorber may be a foreground star-forming galaxy unrelated to the quasar and coincidentally at the same redshift, but our deep imaging and follow-up spectroscopy of the field of Q2343–BX415 has not yet produced a likely candidate. We measure the abundances of 14 elements in the PDLA, finding an overall metallicity of $\sim$1/5 solar and a normal pattern of relative element abundances for this metallicity. Thus, in this PDLA there is no evidence for the supersolar metallicities that have been claimed for some proximate, high-ionization, systems.

Subject headings: cosmology: observations — galaxies: abundances — galaxies: evolution — galaxies: high-redshift — quasars: absorption lines — quasars: individual (Q2343–BX415)

Online material: color figures

1. INTRODUCTION

Absorption line systems at redshifts close to the emission redshift of the quasi-stellar object (QSO) against which they are viewed have traditionally been considered to be somewhat different from the bulk of the truly intervening absorbers and, for this reason, are normally excluded from statistical studies of QSO absorption spectra. Possible differences of these so-called proximate systems compared to "normal" ones may include: (1) they could be produced by material ejected by the quasar or in the host galaxy interstellar medium; (2) their degree of ionization may be influenced by the proximity of the quasar's radiation field (e.g., Foltz et al. 1986); and (3) environmental effects could come into play if the quasars are located in overdense regions (e.g., Sargent et al. 1982). Such reservations also apply to damped Lyman alpha systems, the absorbers at the upper end of the distribution of neutral hydrogen column densities with $N(\mathrm{H\ I}) \geq 2 \times 10^{20}$ cm^{-2} (Wolfe et al. 2005), if located close to the QSO redshift. Indeed, a recent study by Russell et al. (2006) has found that the number density of DLAs almost doubles in the vicinity of QSOs (within 6000 km s^{-1} of the emission redshift), leading those authors to speculate that the excess may result from galaxies in the same cluster or supercluster as the quasar.

While it may therefore be justified to exclude proximate damped Lyman alpha systems, or PDLAs, when considering the statistical properties of DLAs as a whole, the very fact that they may be a different population makes them interesting in their own right. Can we learn more about the quasar environment from PDLAs? Are their chemical properties different from those of intervening DLAs? Supersolar metal abundances have been claimed for gas close to quasar nuclei (Hamann & Ferland 1999; Nagao et al. 2006) and for high-ionization associated systems (Petitjean et al. 1994), but such estimates are much more model dependent than the relatively straightforward determination of element abundances in DLAs (see the discussion by Pettini 2007). Of course there is no reason to assume that all PDLAs have the same origin, and therefore similar properties; indeed some may simply be chance alignments, comparable to the intervening absorbers, while others could form part of the same group or cluster as the QSO, with perhaps only a small fraction originating from the host galaxy itself.

Until recently there have been very few studies of PDLAs, partly because these systems are relatively rare (since DLAs themselves are rare systems), but also because they have often been ignored. While the handful of known cases was boosted slightly with the CORALS survey by Ellison et al. (2002), it is the Sloan Digital Sky Survey (SDSS) that is offering the greatest opportunity to significantly increase the sample size (see e.g., Russell et al. 2006; Prochaska et al. 2007). Consequently it

[1] Based on data obtained at the W. M. Keck Observatory, which is operated as a scientific partnership among the California Institute of Technology, the University of California, and NASA, and was made possible by the generous financial support of the W. M. Keck Foundation.

[2] Isaac Newton Group of Telescopes, Apartado de Correos 321, E-38700 Santa Cruz de La Palma, Canary Islands, Spain.
[3] Institute of Astronomy, Madingley Road, Cambridge, CB3 0HA, UK.
[4] Astronomy Option, California Institute of Technology, MS 105-24, Pasadena, CA 91125.
[5] National Optical Astronomy Observatory, 950 North Cherry Street, Tucson, AZ 85719.
[6] McKinsey and Company, 1420 Fifth Avenue, Suite 3100, Seattle, WA 98101.
[7] Harvard-Smithsonian Center for Astrophysics, 60 Garden Street, Cambridge, MA 02138.
[8] Department of Astrophysical Sciences, Peyton Hall-Ivy Lane, Princeton, NJ 08544.

should soon be possible to examine more generally the statistical properties of the PDLA population.

The few PDLAs studied to date have been found to be broadly similar to other DLAs, although there is some evidence of enhanced Lyα emission (Pettini et al. 1995; Moller & Warren 1993; Moller et al. 1998). This emission has been attributed to various causes, including (1) photoionization from the quasar; (2) the reduced line blanketing from the Lyα forest, due to the proximity effect; and (3) increased star formation in the quasar environment (either directly through gravitational interaction or indirectly due to the fact that quasar activity tends to be located near to galaxies that are actively forming stars). The similarity with intervening DLAs also appears to extend to the chemical properties of the few PDLAs studied so far, which do not appear to be statistically different from the rest of the population of damped absorbers (Akerman et al. 2005; Lu et al. 1996). One difficulty with all of these comparisons, however, is the uncertainty by up to several thousand km s^{-1} in the systemic redshifts of the bright quasars against which PDLAs have been observed; without knowledge of the QSO true redshift, it is not possible to establish whether a proximate system is associated with the QSO environment or is located tens of Mpc in front of it.

1.1. *Q2343–BX415*

In this paper we present observations of a new PDLA in the spectrum of the faint ($\mathcal{R} = 20.22$) $z_{\rm em} = 2.574$ QSO Q2343–BX415 at coordinates $\alpha = 23^{\rm h}46^{\rm m}25.4^{\rm s}$, $\delta = +12^\circ47'44''$ (J2000.0). The QSO and its associated DLA were discovered in the course of a survey for galaxies at $z \sim 2$ in the field of the previously known, brighter ($\mathcal{R} = 17.0$) quasar Q2343+1232 at a similar redshift ($z_{\rm em} = 2.573$); the aim of the survey is to study the connection between star-forming galaxies and the absorption seen in QSO spectra at redshifts $z \simeq 2$–2.5 (Steidel et al. 2004; Adelberger et al. 2005). The discovery spectrum of Q2343–BX415, obtained with the Low Resolution Imaging Spectrograph on the Keck I telescope, revealed the presence of a strong damped Lyα line essentially coincident in redshift with the Lyα emission line, raising the possibility that this PDLA may be associated with the host galaxy of the QSO. Whatever its origin, PDLAs so close in redshift to the background QSO are very rare and warrant further study.

We therefore secured further observations of Q2343–BX415 with the Keck II telescope, in the optical with the Echelle Spectrograph and Imager (ESI; Sheinis et al. 2002), and in the near infrared with the Near Infrared Spectrograph (NIRSPEC; McLean et al. 1998), for the purpose of studying in detail the chemical and kinematic properties of the PDLA and establishing its relationship to the QSO itself. These observations are the subject of the present paper, which is organized as follows. In § 2 we briefly describe the ESI observations and the steps in the data reduction process. In § 3 we give an overall description of the optical spectrum of Q2343–BX415, measure its systemic redshift from the near-IR observations, and derive the column density of the PDLA by decomposing the Lyα line into its emission and absorption components. In § 4 we discuss the kinematics of the metal absorption lines associated with the PDLA, which are found to consist of two sets of components, one redshifted and the other one blueshifted relative to $z_{\rm sys}$. Measurements pertaining to the two sets of components are collected in Table 3. Section 5 deals with the derivation of the abundances of 14 elements in the PDLA, while §§ 6 and 7 examine critically how these abundance determinations may be compromised by, respectively, partial coverage of the QSO continuum by the absorbing gas and the presence of (partly) ionized gas. In § 8 we use the ratio N(C II*)/N(H I) to deduce a conservative limit to the physical distance between the PDLA and Q2343–BX415. We bring all of these findings together in the discussion of § 9.

In addition to the PDLA, our ESI spectrum of Q2343–BX415 includes absorption lines from 11 intervening absorption systems at $z_{\rm abs} < z_{\rm em}$. We catalog them in the Appendix, where we also compare their redshifts to those of galaxies within $\sim 1'$ of the line of sight to Q2343–BX415. Throughout the paper we adopt a cosmology with $\Omega_M = 0.3$, $\Omega_\Lambda = 0.7$, and $H_0 = 70$ km s^{-1} Mpc^{-1}.

2. OBSERVATIONS AND DATA REDUCTION

ESI is a highly suitable instrument for observations of absorption systems in faint QSOs, offering a combination of high-efficiency, wide-wavelength coverage (from 4000 to 10500 Å spread over 10 spectral orders) and a moderately high spectral dispersion of 11.5 km s^{-1} per 15 μm detector pixel. We observed Q2343–BX415 on the nights of 2002 September 4 and 5 for a total exposure time of 15,600 s (four 3600 s exposures + one 1200 s exposure). The atmospheric conditions were mostly clear, with seeing of $\sim 0.6''$ FWHM; the spectrograph slit width was set at $0.75''$ projecting to $\sim$4 CCD pixels.

The individual ESI exposures were reduced with purpose-written IRAF tasks, which implement the conventional steps of bias subtraction, flat-fielding, cosmic-ray rejection, and background subtraction prior to co-adding the individual one-dimensional spectra. Wavelength calibration used the reference spectra of Cu-Ar and Hg-Xe-Ne lamps, and an absolute flux scale was provided by observations of the standard star G191B2B (Oke 1990). The intrinsically smooth spectrum of this white dwarf also allowed us to correct for telluric absorption at red wavelengths.[9] Finally, the QSO spectrum was mapped onto a vacuum heliocentric wavelength scale. For the purpose of studying absorption lines, we fitted the QSO intrinsic spectrum with a spline curve, paying special attention to the fit around the strong emission lines on which resonance absorption lines from the same transition are superposed; division by this spline fit then provided a normalized spectrum suitable for absorption line measurements.

The signal-to-noise ratio of the data varies from S/N $\sim$ 20 to $\sim$170 per 0.25 Å wavelength bin over the interval 5000–9250 Å, being higher in the QSO broad emission lines and in the center of spectral orders, and lower in the continuum and at the edges of orders. It falls to S/N $\sim$ 10 by 4250 Å in the blue and 10,000 Å in the red. The spectral resolution is FWHM $= 45.5 \pm 0.3$ km s^{-1}, sampled with $\sim$4 CCD pixels.

3. THE SPECTRUM OF Q2343–BX415

The reduced ESI spectrum of Q2343–BX415 before normalization is reproduced in Figure 1. In the rest frame of the QSO, at $z_{\rm sys} = 2.57393$ (see § 3.1), our data extend from $\lambda_0 = 1130$ to 2900 Å and include all the familiar ultraviolet emission lines, from Lyα to Mg II λ2798. The strong absorption trough that is superposed on the Lyα emission indicates the presence of a PDLA (see § 3.2). The numerous sharp absorption lines, which are resolved when the spectrum is plotted at higher resolution, correspond to metal absorption lines from the PDLA and from numerous other intervening systems at lower redshifts.

Overplotted on Figure 1 is a portion of the template quasar spectrum produced by Vanden Berk et al. (2001) from the median of over 2200 SDSS QSOs; also shown is the UV-optical continuum approximated by a power law with slope $\alpha_\nu = -0.44$.

[9] We did not apply this correction at wavelengths longward of 9250 Å where S/N < 20.

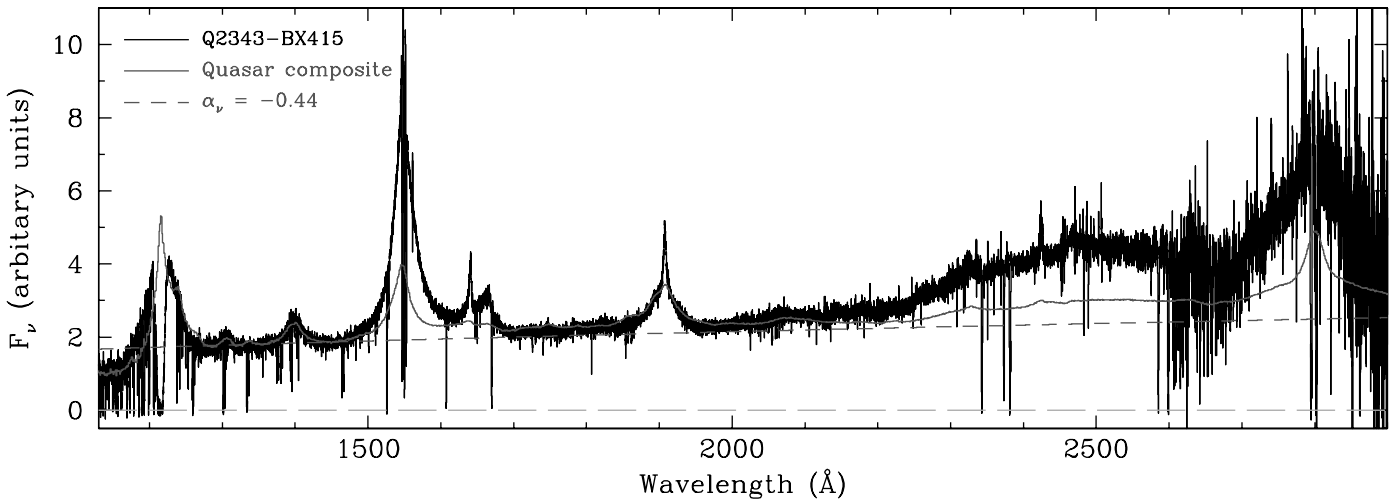

FIG. 1.—Spectrum of Q2343–BX415 (*histogram*) in the systemic rest frame of the quasar ($z_{\rm sys} = 2.57393$). Overplotted is the median composite quasar spectrum from the SDSS (*solid line*; Vanden Berk et al. 2001), along with its best-fitting power-law slope $\alpha_\nu = -0.44$ (*short-dashed line*). The composite spectrum was multiplicatively scaled to compare its continuum slope with that of Q2343–BX415. [*See the electronic edition of the Journal for a color version of this figure.*]

The broad similarity between the two spectra suggests that Q2343–BX415 is a fairly typical quasar. There are differences too, however. In Q2343–BX415, the C IV λ1549 and Mg II λ2798 emission lines are stronger, the Fe II broad emission at wavelengths $\lambda \gtrsim 2200$ Å is also stronger, and there are narrow UV emission lines which, as explained below, help us pin down the systemic redshift of the QSO.

3.1. *The Systemic Redshift of the Quasar*

As we are interested in investigating the relationship between the PDLA and the QSO, it is important to accurately determine their respective redshifts. It has been known for a number of years that in quasars the broad permitted and semiforbidden emission lines are not at the systemic redshift, but are blueshifted by up to several thousand km s^{-1} (see, e.g., Gaskell 1982; Espey et al. 1989). The blueshift is different for different ion stages and shows a strong correlation with ionization energy.

On the other hand, the narrow forbidden lines and the Balmer lines are closer to the systemic redshift, with shifts of less than 100 km s^{-1} (Vanden Berk et al. 2001). In order to measure the redshifts of the [O III] $\lambda\lambda$4959, 5007 doublet and Hβ, we observed Q2343–BX415 in the near-IR *H* band with NIRSPEC on the Keck II telescope, as part of a larger program of near-IR spectroscopy of galaxies and active galactic nuclei (AGNs) at $z \sim 2$ described by Erb et al. (2006). Figure 2 shows the relevant portion of the NIRSPEC spectrum (reduced as described by Erb

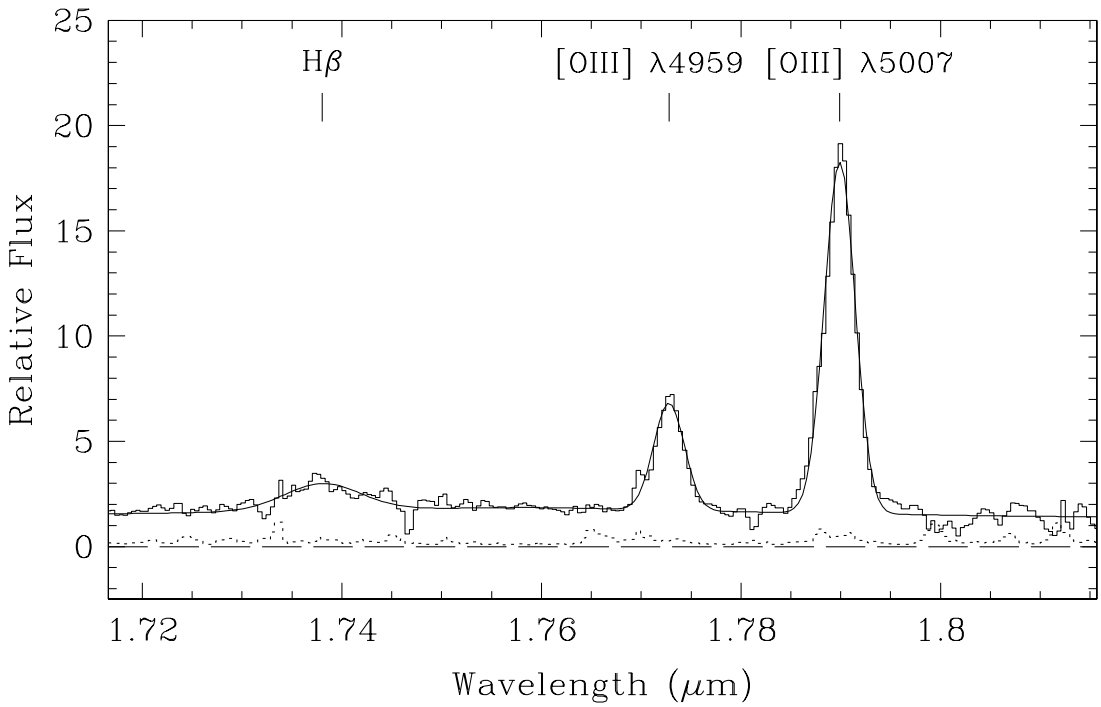

FIG. 2.—Portion of the NIRSPEC spectrum of Q2343–BX415 (*histogram*) and its 1 σ error spectrum (*dotted line*). Overplotted are our Gaussian fits to the [O III] and Hβ emission lines (*solid line*), superposed on the underlying continuum level. The three lines give a mean systemic redshift for the QSO of $\langle z_{\rm sys} \rangle = 2.57393 \pm 0.00005$. [*See the electronic edition of the Journal for a color version of this figure.*]

TABLE 1
THE SYSTEMIC REDSHIFT OF Q2343–BX415

Transition	λ_{vac}[a] (Å)	Instrument	λ_{obs}[b] (Å)	FWHM[c] (km s^{-1})	z_{sys}[d]
He II λ1640[e]	1640.418	ESI	5862.9 ± 0.1	612 ± 19	2.57403 ± 0.00008
C III] $\lambda\lambda$1907, 1909[e]	1907.503:	ESI	6817.8 ± 0.1	493 ± 25	2.57419 ± 0.00007[f]
Hβ	4862.683	NIRSPEC	17380.6 ± 4.3	1550 ± 200	2.57428 ± 0.00088
[O III] λ4959	4960.295	NIRSPEC	17728.0 ± 0.7	570 ± 8	2.57397 ± 0.00014
[O III] λ5007	5008.240	NIRSPEC	17899.1 ± 0.2	570 ± 8	2.57393 ± 0.00004

[a] Vacuum wavelengths of the transition.
[b] Observed central wavelengths of the Gaussian fits.
[c] FWHM of the emission line after correcting for the instrumental resolutions of either 45.5 km s^{-1} (ESI) or 214 km s^{-1} (NIRSPEC).
[d] Systemic redshift.
[e] Both He II λ1640 and C III] $\lambda\lambda$1907,1909 display broad emission features with a narrow component superposed. For the purposes of this analysis we simultaneously fitted both the broad and narrow components, but only quote the fit to the narrow line region.
[f] Uncertainties are introduced into the determination of z_{sys} from C III] due to the unknown intensity ratio between the two lines at 1906.683 and 1908.734 Å, and hence the unknown value of λ_{vac}. Here we assume the regime of low electron densities, where $I(1906.683)/I(1908.734) \rightarrow 1.5$. If the electron density were higher, this ratio would decrease and result in a higher value of λ_{vac} for the blend, and therefore a lower systemic redshift. The FWHM quoted corresponds to the fit over both transitions.

et al. 2006) together with Gaussian fits to the three emission lines; the parameters of the fits are collected in Table 1. From the weighted average of the three redshifts we deduce $\langle z_{sys} \rangle = 2.57393 \pm 0.00005$ (although the measurement is dominated by the narrow [O III] doublet). As can be seen from Table 1, the redshifts of the narrow components of the ultraviolet He II λ1640 and C III] $\lambda\lambda$1907, 1909 emission lines also agree with this value of z_{sys} within the errors.

We also observed the nearby quasar Q2343+1232 in the *H* band with NIRSPEC and measured $z_{sys} = 2.5727 \pm 0.0004$ from its [O III] λ5007 line; thus the two QSOs, which are separated by $\sim$690 kpc on the plane of the sky, have redshifts which differ by only $\sim$100 km s^{-1}. The absorption systems in the optical spectrum of Q2343+1232 have been cataloged by Sargent et al. (1988). They include a C IV system at $z_{abs} = 2.5696$ (which corresponds to a velocity difference $\Delta v = -365$ km s^{-1} from z_{sys} of Q2343–BX415); a DLA at $z_{abs} = 2.4313$ (Lu et al. 1998), which differs by -550 km s^{-1} from the redshift $z_{abs} = 2.4376$ of one of the intervening C IV systems we identify in the spectrum of Q2343–BX415; and a double C IV system at $z_{abs} = 2.1693$, 2.1714, which is also within a few hundred km s^{-1} of a rich concentration of galaxies and absorbing gas near the Q2343–BX415 sight line. As discussed in the Appendix, these velocity similarities attest to the large-scale structure of gas and galaxies at $z \simeq 2$–2.6 seen in this field.

3.2. *The Proximate DLA*

In the top panel of Figure 3 we have reproduced on an expanded scale the portion of Figure 1 that encompasses the Lyα region, so that the blend of emission and damped absorption can be seen clearly. The decomposition of the profile into its components is made easier by the high S/N of the ESI data and the requirement that, once the emission line is divided out, the remaining absorption should exhibit the characteristic Lorentzian shape of the damping wings.

To perform our decomposition, we first subtracted out a fit to the quasar's underlying continuum level, then used the residual spectrum for an initial estimate of the shape and intensity of the Lyα emission line profile. To characterize this emission, we used the ELF (Emission Line Fitting) routines in the Starlink DIPSO data analysis package (Howarth et al. 2004) to fit this estimate with a (multicomponent) Gaussian fit. By dividing the original spectrum by the sum of the quasar's continuum and this emission line fit, it was possible to compare the resulting normalized absorption spectrum with theoretical profiles of damped Lyα lines of varying H I column density, generated by the DIPSO routine HC. Any deviations in the spectra from the theoretical Lorentzian shape were used to modify the original emission line estimate, and the whole cycle was repeated. After several iterations we converged onto a satisfactory solution, shown in the top panel of Figure 3, for which both damping wings and the core of the Lyα line were well fitted by a theoretical profile. Interestingly, we found that *two* Gaussian components, separated by $\sim$600 km s^{-1}, were required for a satisfactory fit to the Lyα emission line[10] (see Fig. 3, *middle*); other relevant parameters are collected in Table 2. The normalized absorption profile is well reproduced by a column density $N(\mathrm{H\ I}) = 9.5 \times 10^{20}$ cm^{-2} (Fig. 3, *bottom*). We found the column density derived to be only weakly sensitive to the precise Lyα emission line profile adopted (despite the varying quality of the overall fit); after many trial fits to the composite of emission and absorption, we estimate the 1 σ error in N(H I) to be of the order of 10%, as indicated in the figure.

In Figures 4*a*–4*g* we have reproduced the rich absorption spectrum of Q2343–BX415 on an expanded scale. We detect 49 transitions from the PDLA due to 14 elements ranging, in the periodic table, from C to Zn and in ionization stages from C I to N V. All these absorption lines are appropriately labeled in Figures 4*a*–4*g*. We also identify 11 other intervening absorption systems, at redshifts lower than that of the DLA; absorption lines from these systems are denoted S1–S11 and are discussed separately in the Appendix.

4. THE KINEMATICS OF THE PDLA

We examine the kinematics of the DLA in Figure 5 by comparing the absorption line profiles of ions in different ionization stages; the zero point of the velocity scale is at $z_{sys} = 2.57393$. The first thing to note is that evidently there are two main clumps of absorption (in velocity space), one receding from the quasar while the other is apparently approaching it. The blueshifted absorption ranges in velocity from +50 to -325 km s^{-1}, while the redshifted components span from +150 to +600 km s^{-1}. Such velocities are of the same order of magnitude as those commonly

[10] To accurately fit the other quasar emission lines observed in the spectrum of Q2343–BX415, for which the line profiles are much better defined, we find that two or three Gaussian components are required.

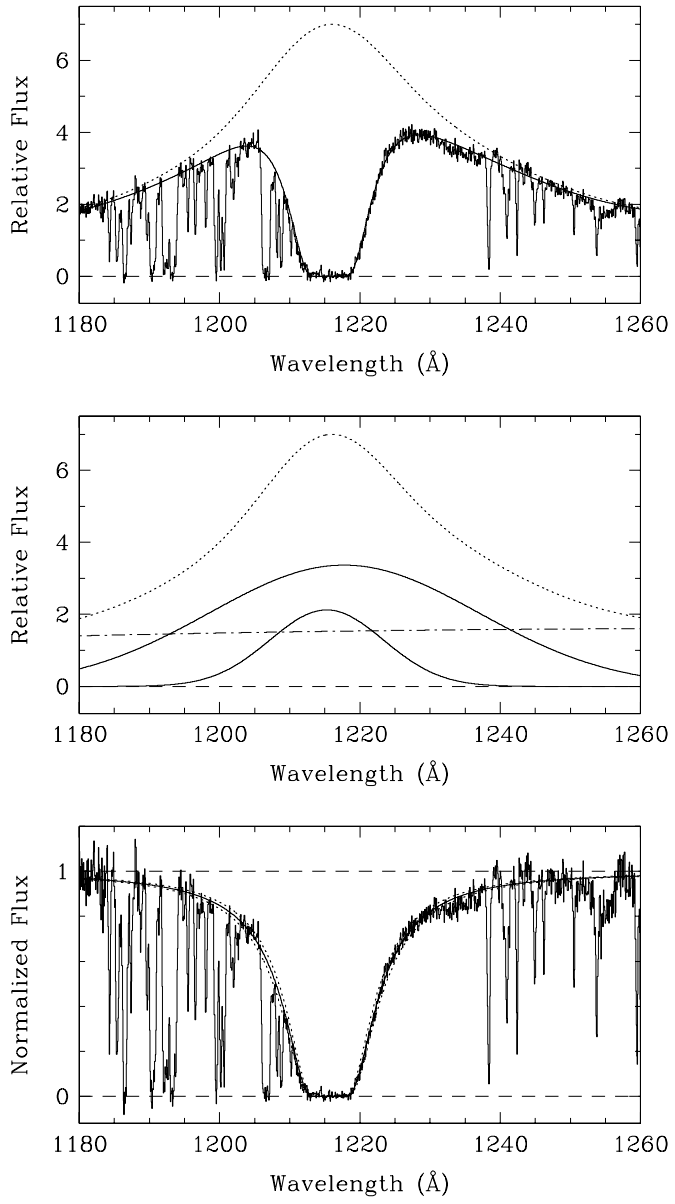

FIG. 3.—The Lyα region in Q2343–BX415. *Top*: The damped Lyα absorption trough of the PDLA superposed on the quasar's Lyα emission line (*histogram*). Overplotted is our reconstruction of the quasar's continuum + Lyα emission line (*dotted line*) and the PDLA's absorption profile for a neutral hydrogen column density $N(\mathrm{H\ I}) = 9.5 \times 10^{20}$ cm^{-2} (*solid line*). *Middle*: Decomposition of the quasar's continuum + Lyα emission line (*dotted line*) into two Gaussian emission components (*solid lines*) and the underlying continuum (*dash-dotted line*). *Bottom*: As for the top panel, but normalized after dividing the observed spectrum by the continuum + Lyα emission line fit. Theoretical damped profiles for column densities $N(\mathrm{H\ I}) = (9.5 \pm 1.0) \times 10^{20}$ cm^{-2} are overplotted on the data (*solid and dotted lines*). [*See the electronic edition of the Journal for a color version of this figure*.]

seen in galactic-scale outflows in star-forming galaxies at redshifts $z \simeq 2$–3 (see, e.g., Pettini et al. 2002b; Erb et al. 2004), raising the possibility that we are witnessing motions of gas associated with the host galaxy of the quasar. Second, while the low and high ions span broadly similar velocity ranges, there are differences in their detailed kinematics, both in the relative strengths of different components and in the velocity where the optical depth is largest. We now discuss these variations in more detail.

In Figure 5 we have chosen Si II λ1526 (*at the top in both columns*) as an example of the absorption by gas that is predominantly neutral (Si II being the dominant ion stage of silicon in H I regions). Moving down each column, we show gas that is increasingly more highly ionized from Al III and Si III, to C IV and Si IV, and finally N V. The first four panels in the right-hand column are particularly useful, as they illustrate the evolution in velocity structure with ionization state for a *single* element, silicon.

TABLE 2

Lyα EMISSION COMPONENTS IN Q2343–BX415

Number	λ_{obs} (Å)	FWHM (km s^{-1})	z_{em}	Δv[a]
1.....	4350.45	11125	2.5786	+390
2.....	4341.61	4701	2.5714	−210

[a] Velocity difference from $z_{\mathrm{sys}} = 2.57393$, determined from [O III] and Hβ (see § 3.1).

Transitions from low ions such as Si II λ1526 show a main component (C1), with peak optical depth at ~ -162 km s^{-1}, blended with weaker one (C2) at ~ -35 km s^{-1}; a third, weakest, component (C3) is centered at $\sim +406$ km s^{-1}. While the Si III λ1206 line is too saturated to discern much information on its velocity structure, the weak Al III $\lambda\lambda$1854, 1862 doublet shows that the strengths of components C2 and C3 relative to C1 increase in moderately ionized gas, although there is little difference (<20 km s^{-1}) in their relative velocities compared to Si II λ1526. The trend continues as we move to Si IV, with C2 and C3 increasing further in strength compared to C1. Furthermore, a fourth component (C4) appears at $\sim +257$ km s^{-1}. The C IV $\lambda\lambda$1548, 1550 lines show the same pattern, even though the individual components are more difficult to disentangle given that the doublet lines' separation, $\Delta v = 499$ km s^{-1}, is comparable to the velocity differences between components. Finally, the N V $\lambda\lambda$1238, 1242 doublet reveals even more pronounced differences in the properties of the very highly ionized gas, with a *single* blueshifted absorber (rather than two components) at ~ -250 km s^{-1}, and two redshifted components of differing widths but centered at similar velocities near $\sim +357$ km s^{-1}, intermediate between those of C3 and C4.

In summary, it appears that the bulk of the neutral gas resides in components C1 and C2, which are receding from the quasar, while ionized gas is more significant in the components that are approaching it (C3 and C4). In Table 3 we have listed separately the equivalent widths of absorption lines in the blueshifted and redshifted components; the velocity ranges over which the equivalent width integration was carried out are given in the fourth column and are indicated by vertical dashed lines in Figure 5.

5. THE CHEMICAL PROPERTIES OF THE PDLA

5.1. *Ion Column Densities*

We derived ion column densities by fitting the absorption lines with multiple Voigt profiles generated by VPFIT (ver. 8.02), a software package that uses χ^2 minimization to deduce the values of redshift z, column density N (cm^{-2}), and Doppler parameter b (km s^{-1}) that best reproduce the observed absorption line profiles. VPFIT[11] takes into account the instrumental broadening function (which in the present case is well approximated by a Gaussian with FWHM = 45.5 km s^{-1}; see § 2) in its χ^2 minimization and error evaluation, and is specifically designed to

[11] VPFIT is available from http://www.ast.cam.ac.uk/~rfc/vpfit.html.

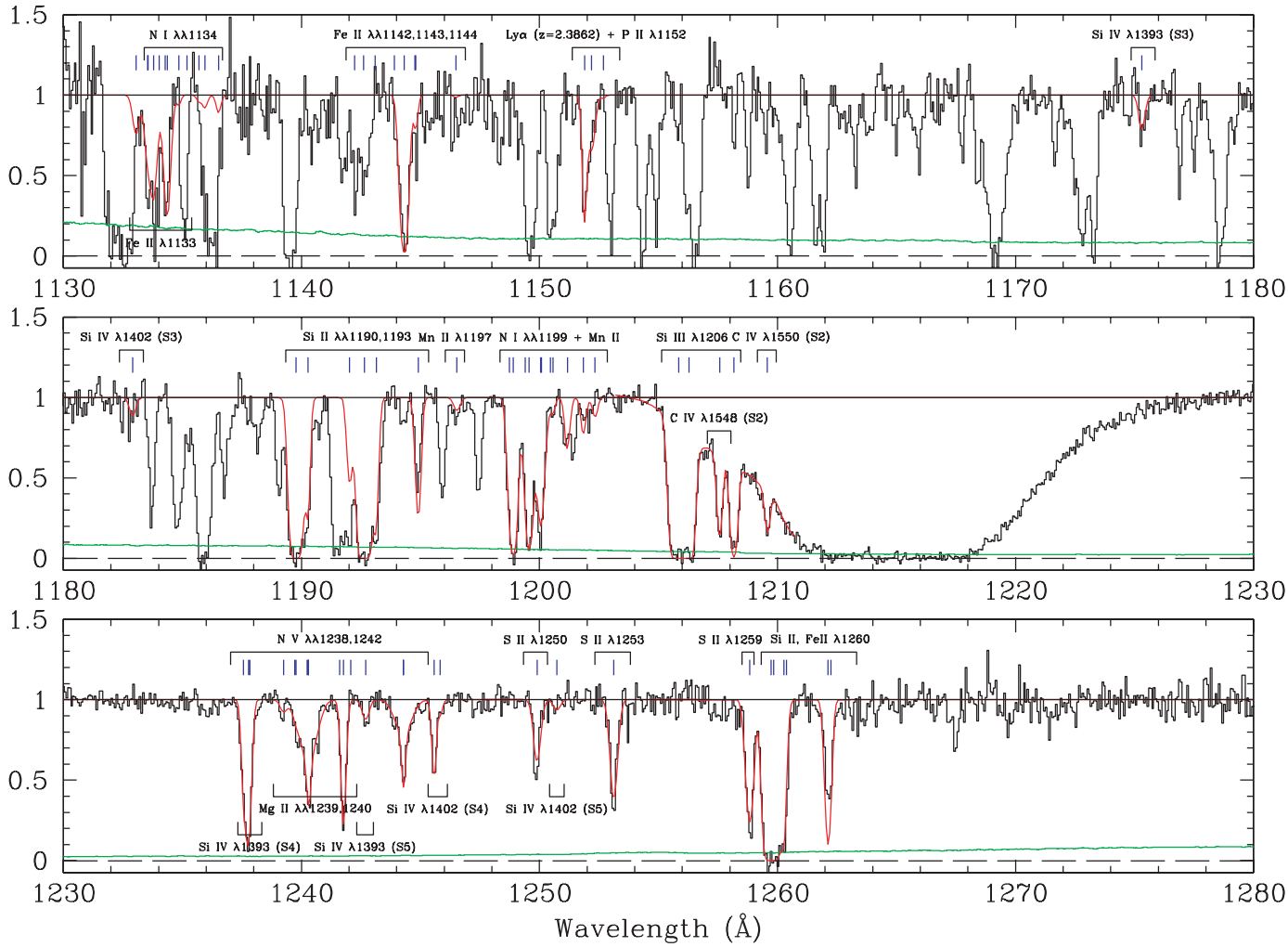

FIG. 4*a*

FIG. 4.—Normalized spectrum of Q2343–BX415 (*black histogram*) in the systemic rest frame of the quasar ($z_{sys} = 2.57393$). The green line near the zero level is the 1 σ error spectrum. Absorption line identifications are given for features originating from (1) the PDLA and (2) any other intervening absorption line systems along the line of sight; the latter are labeled by the system number given in Table 7 (e.g., S4 and S5 in the bottom panel). Overplotted on the spectrum are the absorption line fits from our VPFIT analysis (*red lines*), along with the individual absorption components used in the VPFIT fitting (*blue tick marks*). Blends of lines from different systems were fitted simultaneously.

fit blends of lines (provided there are sufficient constraints). We used the compilation of laboratory wavelengths and *f*-values by Morton (2003) with recent updates by Jenkins & Tripp (2006). The best-fitting line profiles returned by VPFIT are compared with the observed ones in Figures 4*a*–4*g*.

In agreement with our description of the line profiles in § 4, we found that a three-component model was necessary, and sufficient, to characterize the absorption from the low-ionization gas. The kinematic properties of the species that are dominant in H I regions are remarkably uniform: on a first pass in the fitting procedure—when each species is fitted independently of all the others—we found that the redshifts and *b* values returned for each component by VPFIT were in good agreement from ion to ion. We therefore subsequently tied these parameters together for all the low-ionization species, so that each of the three components was characterized by a single value of redshift *z* and Doppler parameter *b*, listed in Table 4. VPFIT was able to converge to an excellent fit for the first two absorption components (C1 and C2). The fitting of C3 (the redshifted component) was much poorer, however, with the absorption being overpredicted for the stronger lines. This is a classic signature of partial coverage, which occurs when the foreground gas does not cover all of the continuum source, suggesting that C3 is physically close to the quasar. We return to this point in § 6 below.

Table 5 lists the column densities fitted for each component, for species that are the dominant ion stages of their respective elements in H I regions. The total column densities, derived by adding together components C1 and C2, are summarized in the final column of the table and again in the second column of Table 6. Inclusion of component C3, which in any case is likely to consist mostly of ionized gas, would increase the column densities of species such as Si II and Fe II by less than 1% (see discussion in § 6). The values for C II, O I, and Al II are lower limits because the corresponding absorption lines are saturated (see Figs. 4*b* and 4*c*); the limits quoted were derived under the assumption that the model parameters listed in Table 4 apply to the saturated lines too. We consider the column density of P II to be an upper limit because of blending with a Lyα forest line (Fig. 4*a*), while Ti II may be marginally detected at the 5 σ level in the $\lambda\lambda$1910.6, 1910.9 doublet (which is unresolved in our data). The value for Mg II is uncertain (as is usually the case in DLAs), because the $\lambda\lambda$2796, 2803 doublet lines are strongly saturated, while those of the $\lambda\lambda$1239.9, 1240.4 doublet are (1) blended with N V $\lambda\lambda$1238, 1242, and (2) so weak as to be very sensitive to the

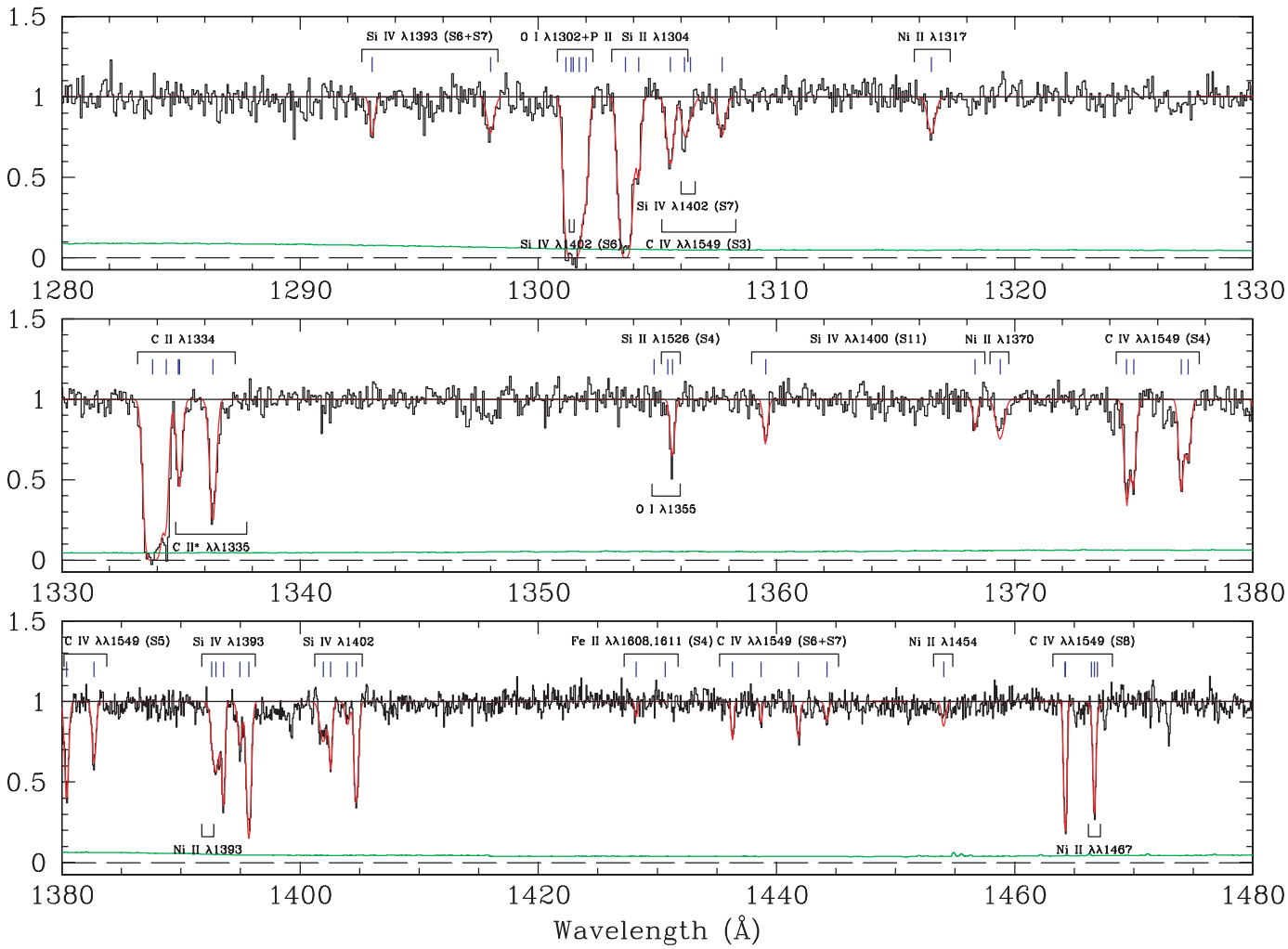

FIG. 4*b*

exact placement of the continuum level in the red wing of the Lyα+N v broad emission line.

5.2. *Element Abundances*

Abundances (or limits) relative to the solar scale (Lodders 2003) are given in the last column of Table 6 for 14 elements in the PDLA under the usual assumption that

$$\log(\mathrm{X/H}) = \log\left(\mathrm{X}^i/\mathrm{H}^0\right), \qquad (1)$$

where X^i is the dominant state of element X in neutral gas. While this approximation has been shown to be appropriate for most intervening DLAs (Vladilo et al. 2001), this may not be the case here, given the proximity of the PDLA to Q2343–BX415. We address this issue in detail in § 7 and conclude that the approximation in equation (1) is in fact valid in the present case too. An additional consideration concerning the accuracy of the abundance measurements in Table 6 is that we have neglected the contribution of molecular hydrogen to the total value of $N(\mathrm{H})$. We have no way of estimating this correction directly, as our ESI spectrum of Q2343–BX415 does not extend below 1130 Å in the rest frame, and therefore does not cover any H_2 absorption lines; however, unless this DLA is very unusual, the fraction of molecular gas is unlikely to be higher than 2% (Petitjean et al. 2006).

The element abundance pattern of the PDLA in Q2343–BX415 is illustrated in Figure 6. The interpretation of such abundance measurements has been discussed extensively in the literature (see, for example, Prochaska et al. 2003; Wolfe et al. 2005); suffice here to say that the observed pattern of element abundances reflects both the previous history of stellar nucleosynthesis and the depletion of refractory elements onto interstellar dust grains. Combining our knowledge of depletions in the interstellar gas of the Milky Way and of element abundances in different stellar populations, it is usually possible to disentangle the two effects. From consideration of the results in Figure 6 we draw the following conclusions:

1. The overall metallicity of the PDLA is $Z_{\mathrm{PDLA}} \simeq \frac{1}{5}-\frac{1}{6}\ Z_{\odot}$, since for the elements that are not usually depleted onto dust we have $[\mathrm{O},\ \mathrm{S},\ \mathrm{Zn/H}] \simeq -0.7$ to -0.8.
2. There appears to be no intrinsic enhancement of alpha-capture elements relative to the Fe group if we take the abundance of the undepleted S and Zn to be representative of, respectively, these two groups of elements: $[\mathrm{S/Zn}] \simeq -0.1$.
3. The underabundances of Ti, Cr, Fe, and Ni relative to Zn (all Fe-peak elements) are most naturally explained as the result of moderate dust depletions, analogous to those observed in diffuse clouds in the halo of the Milky Way (Savage & Sembach 1996). At these modest depletion levels ($[\mathrm{Fe/Zn}] \simeq -0.5$), the finding that Si is not depleted, while Mg apparently is ($[\mathrm{Si/S}] \simeq +0.1$

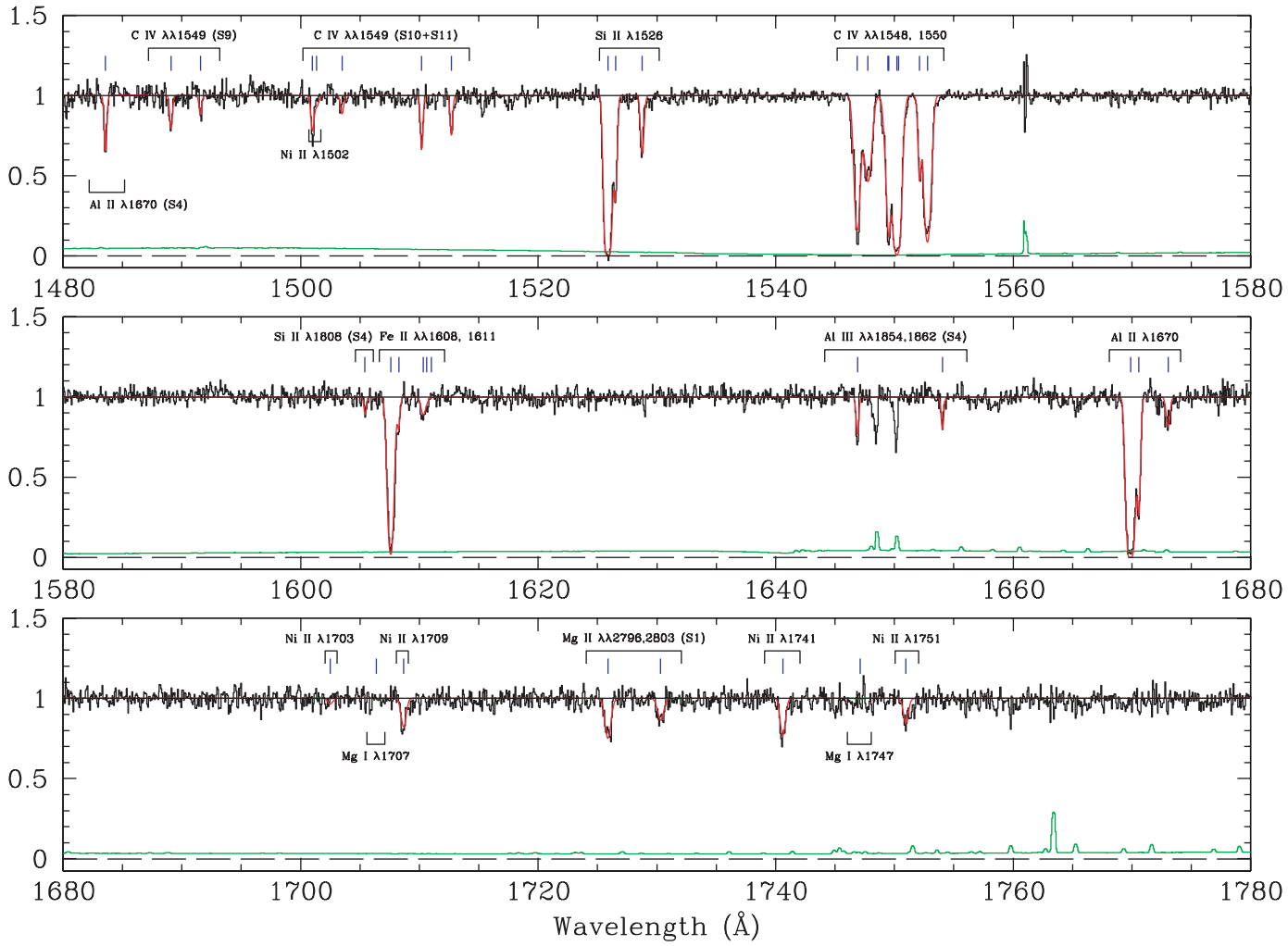

FIG. 4*c*

while [Mg/S] $\simeq -0.24$; all three are alpha-capture elements) is also consistent with analogous measurements in the Galactic ISM (see Table 6 of Savage & Sembach 1996).

4. The enhanced underabundance of Mn probably results from a combination of dust depletion and a genuine decrease in the intrinsic [Mn/Fe] ratio at lower metallicities (Pettini et al. 2000).

5. The element with the lowest abundance is N. While somewhat extreme, the low (N/O) ratio (log (N/O) $\lesssim -1.9$ or [N/O] $\lesssim -1.0$) is nevertheless in the sense expected from the steep dependence of the N production on stellar metallicity (see, for example, the discussion by Pettini et al. 2002a).

However, the most significant conclusion for the purposes of the present study is that findings (1)–(5) are entirely in line with the normal abundance patterns exhibited by most intervening DLAs. This is readily appreciated from inspection of Figures 7 and 8, which compare the metallicity (as measured by [Zn/H]) and the degree of dust depletion (as indicated by the [Cr/Zn] ratio) of the PDLA with the large compilation of analogous measurements assembled by Akerman et al. (2005). It can be seen that, with [Zn/H] $= -0.71$, the metallicity of the PDLA is 2.7 times higher than the median [Zn/H] $= -1.14$ of $\sim$50 DLAs at $z_{\rm abs} = 2$–3, but still well within the range of metallicities encountered in intervening DLAs. Similarly, the depletion of Cr relative to Zn by a factor of $\sim$2 is typical of DLAs with metallicities of $\sim$1/5 solar.

We return to this discussion in § 9 below, after considering the importance of: (1) partial coverage of the QSO continuum, and (2) the QSO ionizing radiation, for the abundance determinations we have just presented. For readers who may not be interested in the details of these calculations, and wish to proceed straight to § 8, the main conclusion of the following two sections is that neither effect is likely to introduce significant corrections to the abundances in Table 6 and Figure 6.

6. PARTIAL COVERAGE

In the course of absorption line fitting (§ 5.1) we found evidence that component C3, which is redshifted relative to $z_{\rm sys}$, does not fully cover the continuum source. We now consider that evidence in more detail. If we examine the PDLA absorption lines in Figures 4*a*–4*g* and most directly in the top panels of Figure 5, it is obvious that the component with the highest optical depth in the species that are dominant in H I regions—component C1 centered at $v = -162$ km s^{-1} relative to $z_{\rm sys} = 2.57393$ (see Table 4)—has no residual flux in the core of the strongest absorption lines. The damped Lyα line itself shows no discernible flux leaking in the line core within the accuracy with which the background level can be determined; clearly this

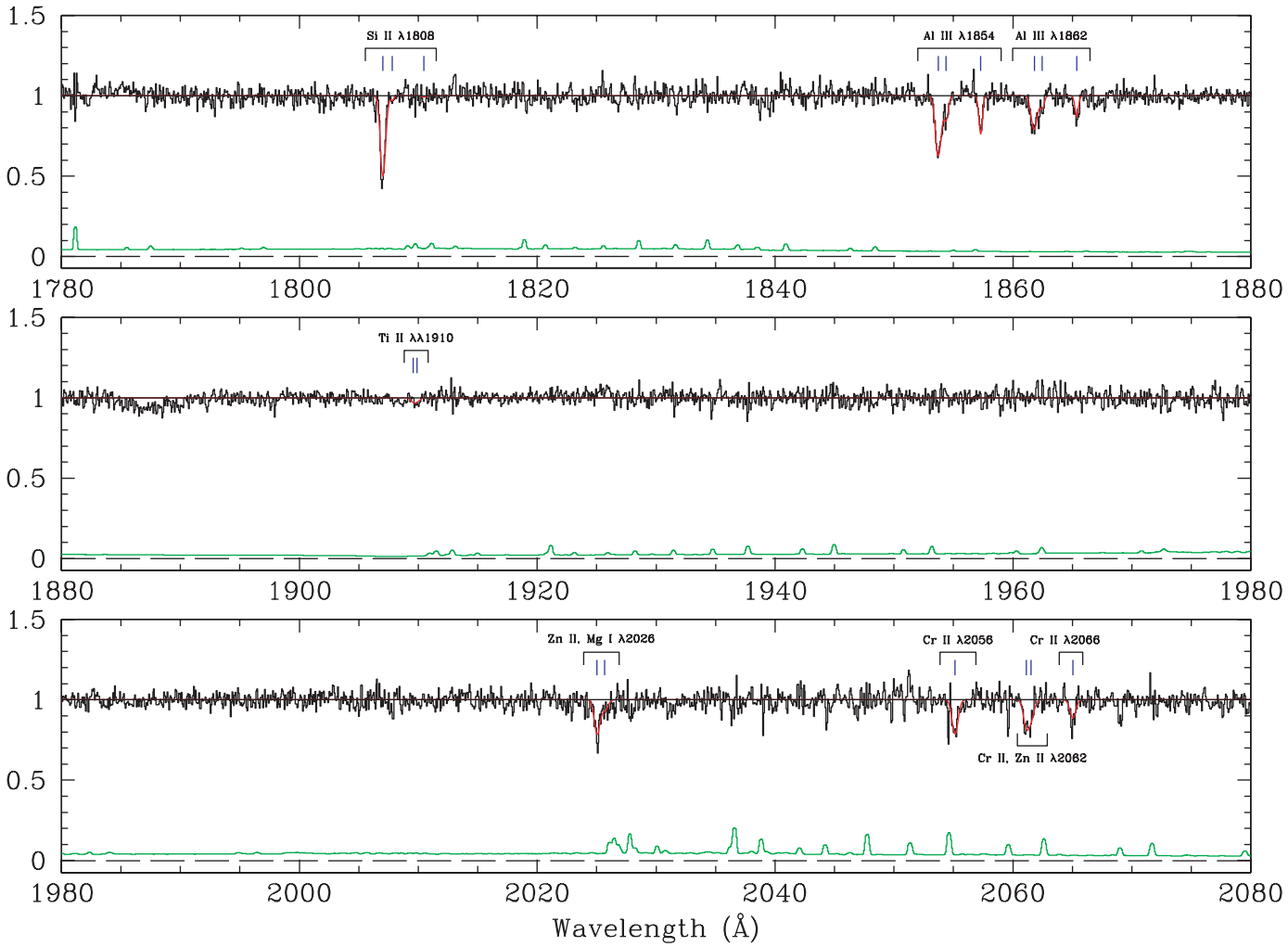

FIG. 4*d*

component must completely cover not only the continuum emitting region but also the more extended broad emission line region. On the other hand, the redshifted absorption at velocities between $v = +150$ and $+600$ km s^{-1} does not reach below $\sim$0.2 of the continuum flux in any of the transitions covered by the 45.5 km s^{-1} resolution ESI spectrum, nor could it be fitted satisfactorily with VPFIT.

We can address this issue more quantitatively by examining the run of apparent optical depth with velocity for transitions that arise from the same ground state of a given ion. The apparent column density of an ion in each velocity bin, $N_a(v)$ in units of cm^{-2} (km s^{-1})$^{-1}$, is related to the apparent optical depth in that bin $\tau_a(v)$ by the expression

$$N_a(v) = \frac{\tau_a(v)}{f\lambda}\frac{m_e c}{\pi e^2} = \frac{\tau_a(v)}{f\lambda(\text{Å})}3.768 \times 10^{14}, \qquad (2)$$

where the symbols f, λ, c, e, and m_e have their usual meanings. The apparent optical depth can be deduced directly from the observed intensity in the line at velocity v, $I_{\rm obs}(v)$, by

$$\tau_a(v) = -\ln[I_{\rm obs}(v)/I_0(v)], \qquad (3)$$

where $I_0(v)$ is the intensity in the continuum. With the assumption of negligible smearing of the intrinsic line profile by the instrumental broadening function, we can approximate

$$\tau_a(v) \approx \tau(v), \qquad (4)$$

where $\tau(v)$ is the true optical depth. The run of $N_a(v)$ with v should be the same, within the errors in $I_{\rm obs}(v)$, for all lines arising from the same atomic energy level, provided there are no unresolved saturated components to the absorption lines and the covering factor is unity (Savage & Sembach 1991). The assumption in equation (4) is probably not justified in our case: observations of damped Lyman alpha systems at $\sim$6 km s^{-1} resolution show that absorption components much narrower than the 45.5 km s^{-1} resolution of the ESI data presented here are not unusual (Wolfe et al. 2005). Even so, lack of agreement in $N_a(v)$ between different transitions would still be an indication of saturation or partial coverage,[12] although the opposite may not be true.

[12] In the following discussion, we use the nomenclature *saturation* to refer to line saturation arising in the "typical" scenario that the intervening gas has a uniform covering factor ($f = 1$), while *partial coverage* is adopted for cases where there is a nonuniform covering factor. Note that the latter definition does not exclude the possibility that the absorption lines also suffer from saturation.

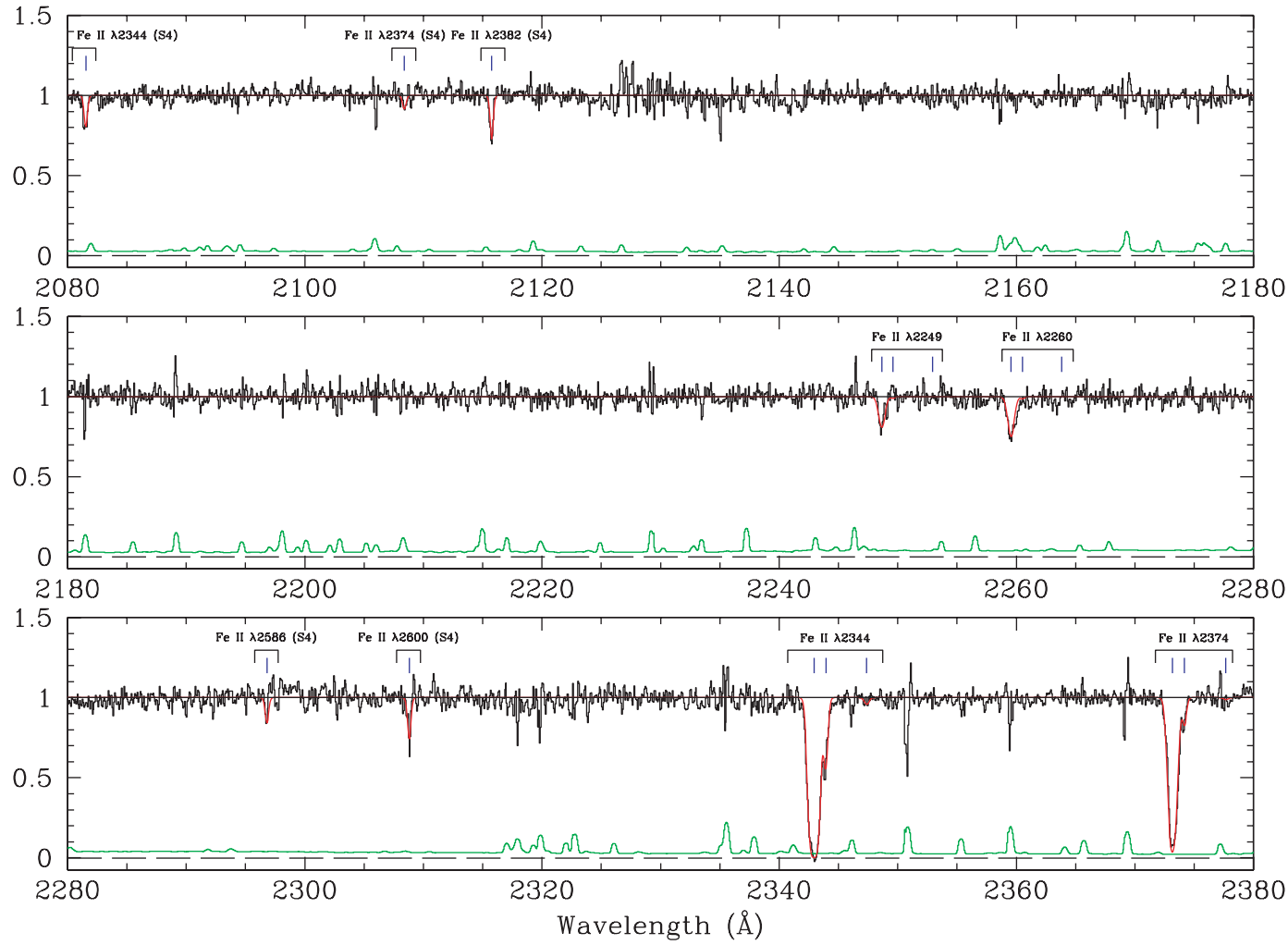

FIG. 4*e*

Among the ion transitions covered in our spectrum of Q2343–BX415, there are three doublets whose apparent optical depths can be compared over the full velocity range of the absorption (or nearly so): Al III, Si IV, and N V; in all other cases either the main absorption component is saturated, or the redshifted absorption is too weak, or one of the lines is seriously affected by blending. Values of $N_a(v)$ for the three doublets are shown in Figure 9. For Al III and Si IV we see good agreement, within the noise, in the blueshifted absorption (components C1 and C2), but not in the redshifted absorption (C3). The situation is less clear cut in N V, where there may be disagreement in the values of $N_a(v)$ between the two members of the doublet in both the blueshifted and redshifted components. As noted earlier, N V is displaced in velocity relative to Al III, Si IV, and C IV, attesting to the complex nature of the absorbing gas.

When it comes to species that are the dominant ions in H I regions and on which the abundance analysis in § 5.2 was based, we can only perform the optical depth consistency check on individual components, rather than on the full range of the absorption, for the reasons given above. Even so, the illustrative comparisons reproduced in Figure 10 are instructive. Component C1 is well behaved in S II (*top*), while C3 again shows evidence of saturation or partial coverage in Si II (*middle*) and Mg II (*bottom*).

We argue that the discrepancies in the $N_a(v)$ profiles of C3 most likely arise from partial coverage, rather than simply from saturation, for the following reasons. First, we consider the higher ionization Al III lines, for which we can directly compare the profiles of both blueshifted and redshifted absorption. If the discrepancy observed in the *weaker* redshifted component were due to saturation, the stronger blueshifted components would also be saturated and should display discrepancies in the line profiles, in contrast with what is observed. It therefore appears that the third, redshifted, component of the moderately ionized gas suffers from partial coverage. Of course we cannot be certain that the lower ionization gas is spatially coincident with the higher ionization gas. Nevertheless, it seems unlikely that the discrepancies in $N_a(v)$ observed for the low-ionization gas are due to saturation, as no discrepancy is seen for the main component of Si IV λ1393 (see Fig. 9), which has a comparable optical depth to the third components of some of the Si II and Mg II lines.

To summarize, it appears that the geometrical distribution of the blueshifted and redshifted absorptions are different, with the former totally covering the QSO continuum and broad line emitting regions, while the latter only does so partially or inhomogeneously. If a significant fraction of the neutral gas resided in the redshifted component C3, the element abundances we deduced in § 5.2 may have been underestimated. Fortunately, C3 accounts for negligible amounts of the ions that are dominant in H I regions. Based on the lines with the lowest values of $f\lambda$ in which C3 is seen (these are the lines where the effect of partial

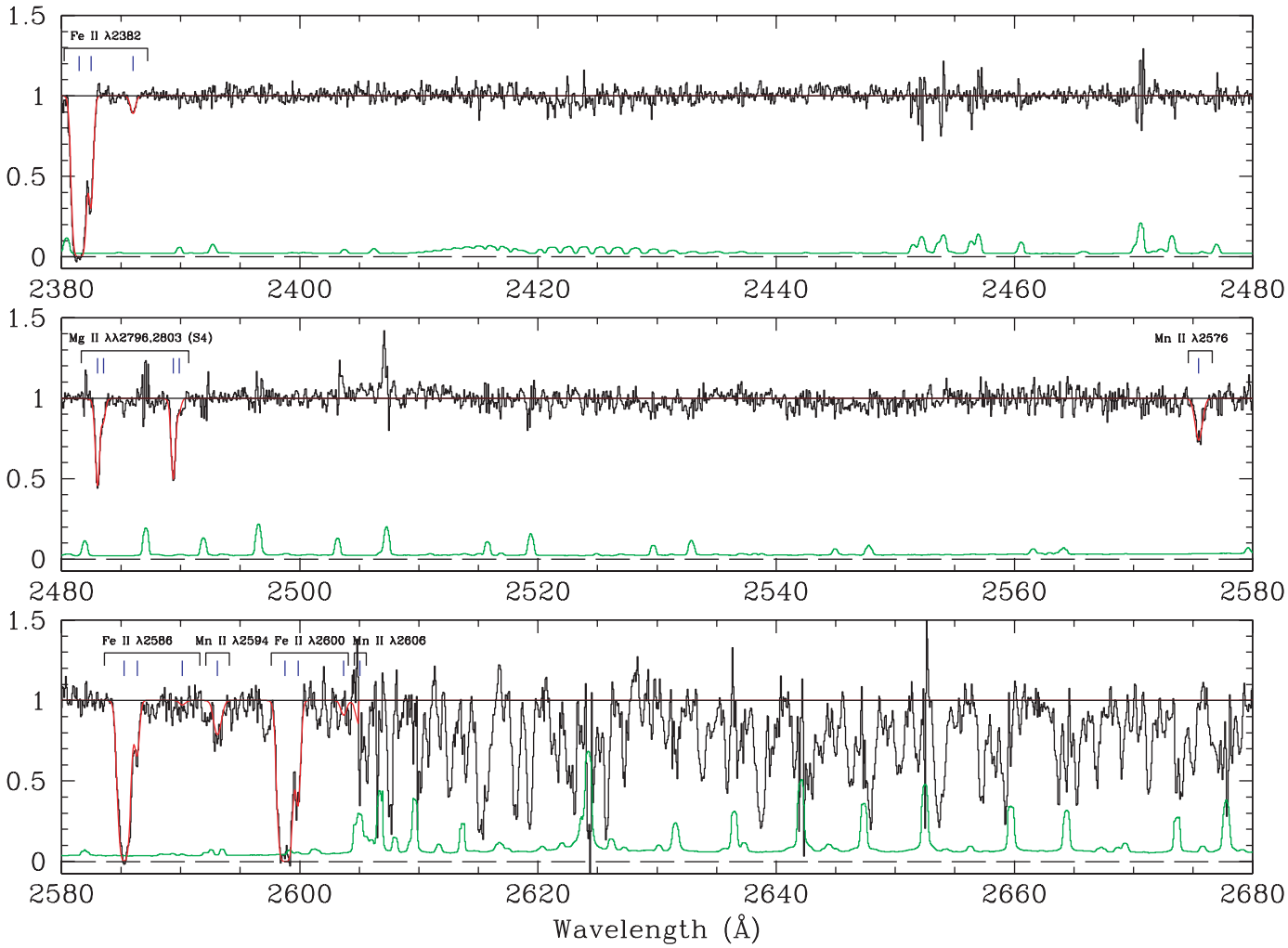

FIG. 4*f*

coverage on the derivation of the column density is minimized), we estimate from the optical depth and line fitting analyses that the fraction of N(Mg II), N(Si II), and N(Fe II) contributed by C3 is in all three cases $\lesssim$1%.

7. IONIZATION CORRECTIONS

In § 5.2 we derived element abundances by relating the column density of each element *in its dominant ionization state in neutral gas* to that of neutral hydrogen. Referring to equation (1), this assumption neglects the possibility that the line of sight may include (partly) ionized gas where $N(\mathrm{X}^i)/N(\mathrm{H\ I}) \neq N(\mathrm{X})/N(\mathrm{H})$. For example, a fraction of the column density $N(\mathrm{X}^i)$ may arise in ionized gas, leading to an *overestimate* of the true abundance of element X; or an element may be overionized compared with H, resulting in an *underestimate* of its abundance.

This has been a potential problem for interstellar abundance studies since their very beginning (e.g., Steigman et al. 1975). Vladilo et al. (2001) considered the issue in depth for intervening DLAs exposed to the metagalactic ionizing background and stellar UV radiation from their host galaxies. The principal conclusion of that work was that for most DLAs the contamination from H II regions leads to abundance corrections that are generally less than 0.1–0.2 dex, smaller than, or comparable to, other sources of error.

In proximate DLAs, however, the corrections may well be larger, depending on the impact of the QSO's own radiation on the ionization structure of the gas. We examined this possibility closely by running a series of photoionization models with the software package CLOUDY (ver. 05.07.06; Ferland et al. 1998; Ferland 2000).[13] The PDLA is treated as a slab of gas of constant density on which a variety of radiation fields are impinging. For Q2343–BX415 itself we adopted an AGN ionizing continuum with a power-law slope $\alpha_\nu = -0.44$ (see § 3); in addition, we included the metagalactic ionizing background (Haardt & Madau 2001) and the cosmic microwave background, both at $z = 2.572$, as well as cosmic-ray ionization at a level comparable to that in our own Galaxy. We adjusted the CLOUDY element abundance scale to reflect the abundance pattern determined in § 5.2, which is a mixture of genuine underabundances and dust depletions, and added dust grains in the right proportions to reflect the latter.

We ran a grid of CLOUDY models by varying two parameters: the gas density ($\log [n(\mathrm{H})/\mathrm{cm}^{-3}] = -3$ to +3) and the ionization parameter ($\log U = -5$ to +1).[14] For each combination of n(H) and U we stopped the calculation once the measured column density of neutral gas, $N(\mathrm{H\ I}) = 9.5 \times 10^{20}$ cm^{-2} (§ 3.2), was reached, and then computed the distance, for each element

[13] See http://www.nublado.org.

[14] The ionization parameter U used by CLOUDY is the dimensionless ratio between the hydrogen ionizing photon density and the gas density. It can be expressed as $U = \phi(\mathrm{H})/n(\mathrm{H})c$, where ϕ(H) is the surface flux of ionizing photons, n(H) is the total hydrogen density and c is the speed of light.

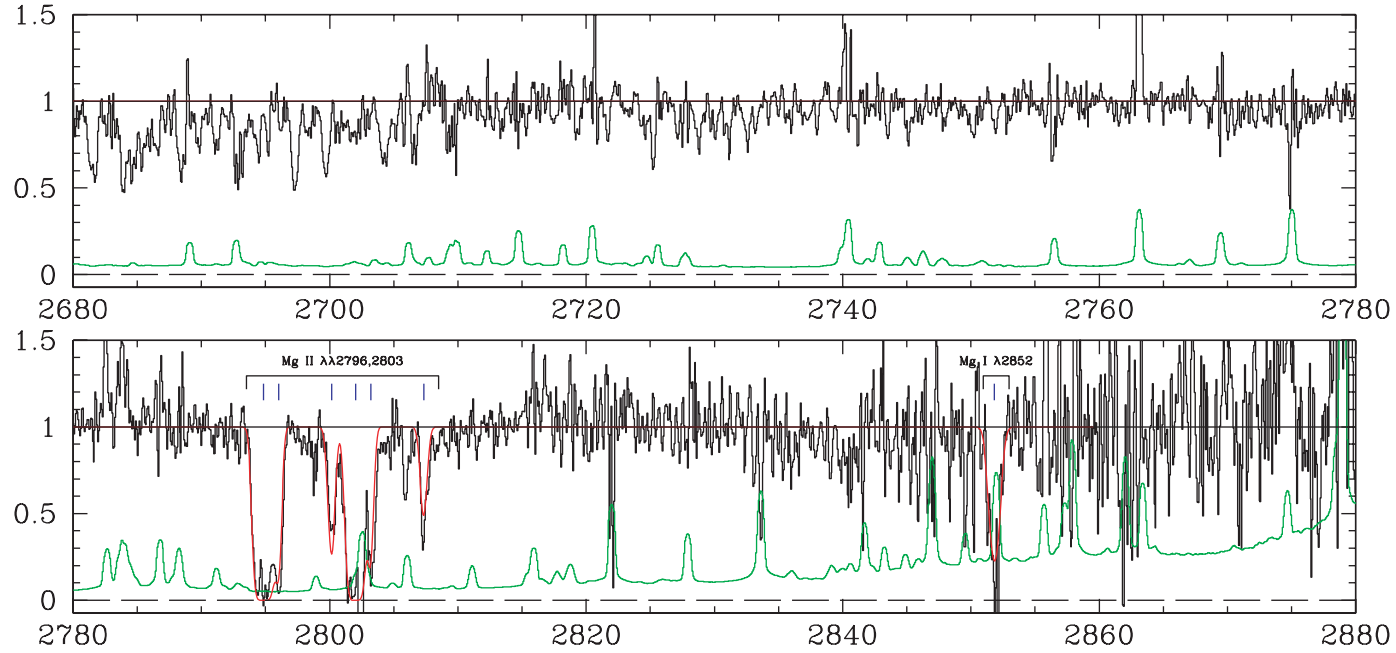

FIG. 4*g*

observed, between the input abundance and the abundance that would be deduced by applying the assumption of equation (1). This defines an ionization correction

$$\mathrm{IC(X)} = \log\left[\frac{N(\mathrm{X})}{N(\mathrm{H})}\right]_{\mathrm{intrinsic}} - \log\left[\frac{N(\mathrm{X}^i)}{N(\mathrm{H\ I})}\right]_{\mathrm{computed}}, \quad (5)$$

which is negative when the abundance of an element has been overestimated by neglecting the ionized gas.

Figure 11 shows the magnitude of such ionization corrections for different elements as a function of log U for a representative case with $\log[n(\mathrm{H})/\mathrm{cm}^{-3}] = +1$; the results for other values of gas density are qualitatively similar. Clearly, the impact of the ionization corrections on our estimates of element abundances depends sensitively on the value of the ionization parameter, at least for some elements. In order to make progress it is therefore necessary to pin down, or at least constrain, the value of U.

This can be achieved by considering the ratios of different ionization stages of the same element; as found by Vladilo et al. (2001), the ratio of Al III and Al II is of particular diagnostic value in this context. This is illustrated in Figure 12, where the values of $\log[N(\mathrm{Al\ III})/N(\mathrm{Al\ II})]$ computed by CLOUDY are color coded as a function of both U and $n(\mathrm{H})$; clearly the major dependence is on U (in the sense that the ratio increases with the ionization parameter) rather than $n(\mathrm{H})$.

Referring to Figures 4*c* and 4*d*, respectively, it can be seen that while Al II λ1670 is saturated, the lines of the Al III $\lambda\lambda$1854, 1862 doublet are weak. Profile fitting with VPFIT (*shown in red in the figures*), gives $N(\mathrm{Al\ III}) = 2.1 \times 10^{13}$ cm^{-2} and $N(\mathrm{Al\ II}) \geq 3.7 \times 10^{14}$ cm^{-2} for components C1 and C2,[15] from which we deduce

$$\left[\frac{N(\mathrm{Al\ III})}{N(\mathrm{Al\ II})}\right]_{\mathrm{observed}} \leq 10^{-1.25}. \quad (6)$$

From Figure 12 we find that such low ratios can only be achieved (in the broad parameter space that we explored) if $\log U \lesssim -4.3$. This in turn implies small ionization corrections: $\mathrm{IC(X)} < 0.1$ for all elements apart from Zn (Fig. 11).[16]

It is remarkable that the Al III/Al II ratio is so low, given the proximity of Q2343–BX415 to the DLA. The ratio we measured here is, if anything, toward the lower end of the distribution of values found in conventional DLAs at $z_{\mathrm{abs}} \ll z_{\mathrm{em}}$ (see Fig. 2 of Vladilo et al. 2001). Evidently, the neutral gas in this PDLA is shielded from the additional ionizing radiation provided by the nearby quasar. Even though there is absorption by a range of ionization stages over the same velocity intervals (see Fig. 5), the ionized and neutral gas presumably occur in physically distinct regions. For the purposes of the present discussion, we conclude that the element abundance analysis presented in § 5.2 is unlikely to be in serious error as a result of the proximity of the DLA to the background QSO.

8. THE DISTANCE OF THE PDLA FROM Q2343–BX415

Among the absorption lines we detect in the PDLA is C II* λ1335.7032, which arises from the excited fine-structure $^2P_{3/2}$ level of the ground state of singly ionized carbon. The absorption line can be seen clearly in the middle panel of Figure 4*b*. Attention has focused on this line in DLAs since Wolfe et al. (2003) pointed out that it could be used to infer the strength of the radiation field to which the gas is exposed. Briefly, the argument is based on the fact that the spontaneous downward transition to the $^2P_{1/2}$ ground state (from which the stronger C II λ1334.5323 absorption line arises) at 158 μm is likely to be the major coolant in H I regions. In thermal equilibrium, the cooling rate is expected to balance the heating rate; since the latter is primarily due to photoelectric emission from dust grains, the cooling rate inferred from the ratio $N(\mathrm{C\ II^*})/N(\mathrm{H\ I})$ can be used to

[15] The first (second) component of Al III was fitted with a column density $N = 1.7 \times 10^{13}$ cm^{-2} (4.0×10^{12} cm^{-2}), Doppler parameter $b = 48.9$ km s^{-1} (26.5 km s^{-1}), and redshift $z = 2.57203$ (2.57330).

[16] It has been suspected for some time that there may be problems with the ionization balance computed by CLOUDY for Zn (e.g., Howk & Sembach 1999; Vladilo et al. 2001), presumably as a result of incorrect atomic data relevant to the calculations of the ionization and recombination rates.

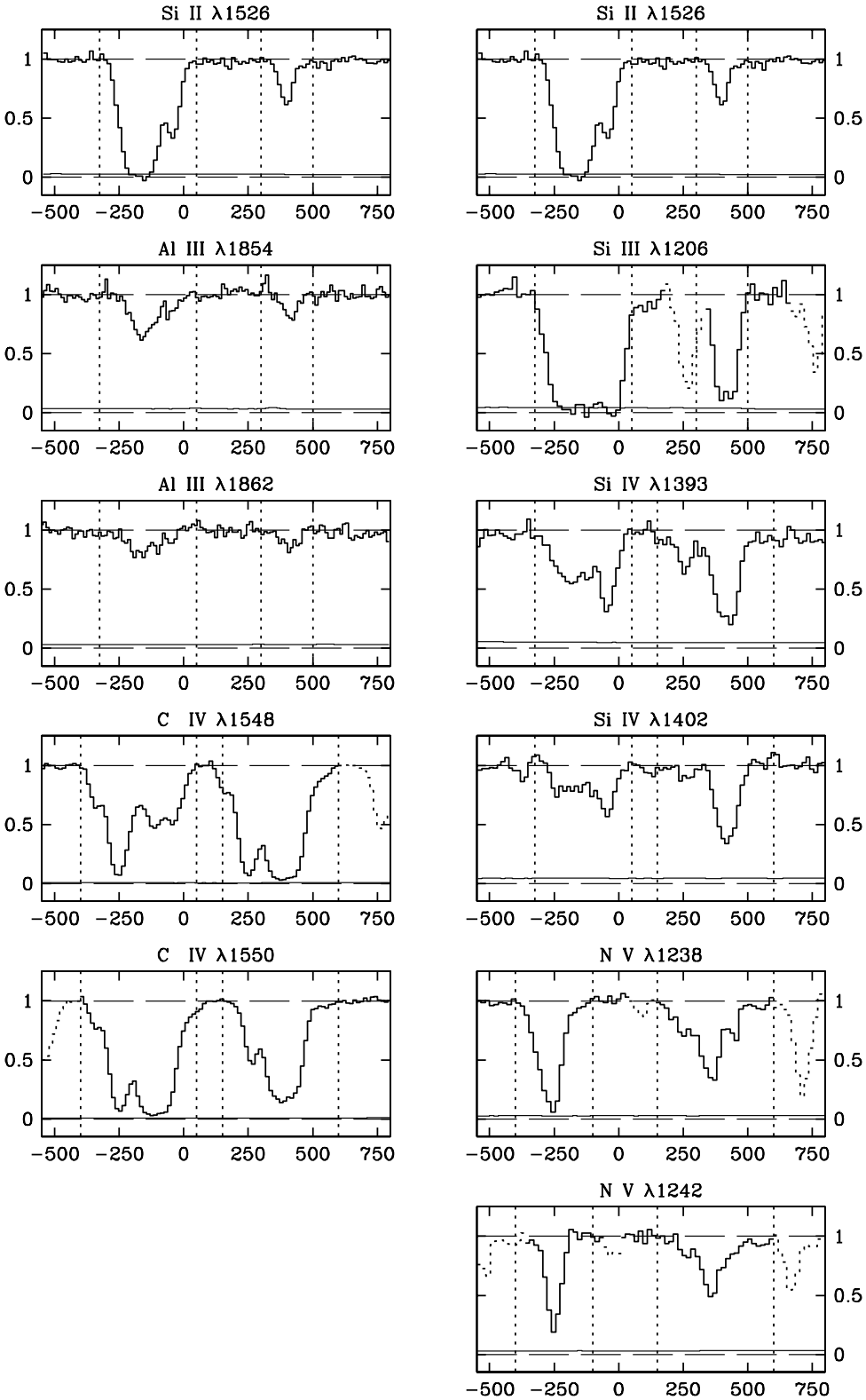

FIG. 5.—Velocity structure of the PDLA's absorbing gas and its dependence on ionization level. Each plot shows the normalized absorption profile for a particular species (*histogram*); the line near the zero level is the corresponding 1 σ error spectrum. The x-axis is velocity (in km s^{-1}) relative to $z_{\rm sys} = 2.57393$; the y-axis is residual flux. Blending with lines from other species is flagged by a dotted line. In addition, note that the redshifted component of C IV λ1548 is blended with the blueshifted component of C IV λ1550, since the doublet lines' separation is 499 km s^{-1}. The dashed vertical lines indicate the two wavelength ranges over which the equivalent widths listed in Table 3 were measured. [*See the electronic edition of the Journal for a color version of this figure*.]

TABLE 3
PDLA Absorption Lines

Ion	λ_{lab}[a] (Å)	f[a]	Δv[b] (km s^{-1})	λ_{obs}[c] (Å)	z_{abs}[d]	W_0[e] (Å)	σ[f] (Å)	Comments
Low-Ionization Species: Blueshifted Components								
N I	1134.656	0.0849	−455 to +135	4053.10	2.5721	1.00	0.07	Refers to N I λ1134 triplet; upper limit
Fe II	1144.9379	0.0830	−325 to +50	4090.03	2.5723	0.54	0.04	...
P II	1152.8180	0.245	−250 to −50	4117.37	2.5716	0.22	0.02	Upper limit, blended with Lyα
Si II	1190.4158	0.292	−325 to +50	4252.40	2.5722	1.05	0.02	Upper limit as blended
Si II	1193.2897	0.582	−325 to +50	4262.58	2.5721	1.20	0.02	Upper limit as blended
N I	1199.967	0.262	−430 to +235	4286.71	2.5724	1.27	0.02	Refers to N I λ1199 triplet
S II	1250.578	0.00543	−250 to −50	4467.09	2.5720	0.14	0.01	...
S II	1253.805	0.0109	−250 to −50	4478.53	2.5719	0.23	0.01	...
S II	1259.518	0.0166	−250 to −50	4499.20	2.5722	0.36	0.01	Upper limit, blended with Si II λ 1260
Si II	1260.4221	1.18	−325 to +50	4502.63	2.5723	1.15	0.02	Upper limit, blended with S II λ 1259
O I	1302.1685	0.0480	−325 to +50	4651.62	2.5722	1.01	0.02	...
Si II	1304.3702	0.0863	−325 to +50	4659.47	2.5722	0.78	0.02	Upper limit, blended with O I λ 1302
Ni II	1317.217	0.0571	−250 to −50	4705.10	2.5720	0.09	0.01	...
C II	1334.5323	0.128	−325 to +50	4767.44	2.5724	1.15	0.02	...
C II*	1335.7032	0.1278	−250 to −50	4771.00	2.5719	0.19	0.01	...
Ni II	1370.132	0.0588	−250 to −50	4894.39	2.5722	0.09	0.02	...
Si II	1526.7070	0.133	−325 to +50	5453.74	2.5722	1.06	0.01	...
Fe II	1608.4511	0.0577	−325 to +50	5745.66	2.5722	0.73	0.01	...
Al II	1670.7886	1.74	−325 to +50	5968.50	2.5723	1.17	0.02	...
Ni II	1709.6042	0.0324	−250 to −50	6106.92	2.5721	0.11	0.01	...
Ni II	1741.5531	0.0427	−250 to −50	6220.89	2.5720	0.14	0.01	...
Ni II	1751.9157	0.0277	−250 to −50	6258.17	2.5722	0.11	0.01	...
Si II	1808.0129	0.00208	−250 to −50	6458.18	2.5720	0.25	0.01	...
Ti II	1910.764	0.202	−250 to −50	...	...	$\leq$0.025	...	5 σ upper limit
Zn II	2026.1370	0.501	−250 to −50	7237.65	2.5721	0.16	0.01	Upper limit, blended with Mg I λ 2026
Cr II	2056.2569	0.103	−250 to −50	7344.79	2.5719	0.14	0.03	Noisy
Cr II	2062.2361	0.0759	−250 to −50	7366.69	2.5722	0.14	0.01	Upper limit, blended with Zn II λ 2062
Cr II	2066.1640	0.0512	−250 to −50	7379.98	2.5718	0.07	0.01	...
Fe II	2249.8768	0.00182	−250 to −50	8036.58	2.5720	0.10	0.01	...
Fe II	2260.7805	0.00244	−250 to −50	8075.80	2.5721	0.22	0.01	...
Fe II	2344.2139	0.114	−325 to +50	8373.97	2.5722	1.42	0.01	...
Fe II	2374.4612	0.0313	−325 to +50	8481.89	2.5721	0.98	0.01	...
Fe II	2382.7652	0.320	−325 to +50	8511.75	2.5722	1.70	0.02	...
Mn II	2576.877	0.361	−250 to −50	9204.81	2.5721	0.19	0.01	...
Fe II	2586.6500	0.0691	−325 to +50	9240.12	2.5722	1.40	0.02	...
Mn II	2594.499	0.280	−250 to −50	9267.56	2.5720	0.23	0.02	Noisy
Fe II	2600.1729	0.239	−325 to +50	9288.40	2.5722	1.73	0.02	Upper limit as blended
Mg II	2796.3543	0.6155	−325 to +50	9989.64	2.5724	2.27	0.03	...
Mg II	2803.5315	0.3058	−325 to +50	10015.06	2.5723	2.43	0.09	Extremely noisy
Mg I	2852.9631	1.83	−325 to +50	10191.84	2.5724	0.98	0.18	Extremely noisy
Low-Ionization Species: Redshifted Components								
Si II	1193.2897	0.582	+300 to +500	4270.39	2.5787	0.15	0.02	...
N I	1199.967	0.262	+195 to +685	4293.88	2.5783	0.25	0.02	Refers to N I λ1199 triplet
Si II	1260.4221	1.18	+300 to +500	4510.79	2.5788	0.25	0.01	...
C II	1334.5323	0.128	+300 to +500	4776.04	2.5788	0.28	0.01	...
Si II	1526.7070	0.133	+300 to +500	5463.67	2.5787	0.13	0.01	...
Fe II	1608.4511	0.0577	+300 to +500	5755.34	2.5782	0.07	0.01	Upper limit, blended with Fe II λ1611
Al II	1670.7886	1.74	+300 to +500	5979.17	2.5787	0.10	0.01	...
Fe II	2382.7652	0.320	+300 to +500	8527.38	2.5788	0.06	0.01	...
Mg II	2796.3543	0.6155	+300 to +500	10008.06	2.5790	0.54	0.03	Upper limit
Mg II	2803.5315	0.3058	+300 to +500	10033.37	2.5788	0.46	0.03	Upper limit
High-Ionization Species: Blueshifted Components								
Si III	1206.500	1.63	−325 to +50	4310.11	2.5724	1.23	0.02	...
N V	1238.821	0.1560	−400 to −100	4423.54	2.5708	0.42	0.01	...
N V	1242.804	0.07770	−400 to −100	4437.84	2.5708	0.22	0.01	Upper limit, blended with N V λ1238
Si IV	1393.7602	0.513	−325 to +50	4979.13	2.5724	0.57	0.02	...
Si IV	1402.7729	0.254	−325 to +50	5011.57	2.5726	0.29	0.02	...
C IV	1548.204	0.1899	−400 to +50	5529.73	2.5717	0.99	0.00	...
C IV	1550.781	0.09475	−400 to +50	5539.46	2.5720	1.36	0.00	Upper limit, blended with C IV λ1548
Al III	1854.7184	0.559	−325 to +50	6625.72	2.5724	0.28	0.01	...
Al III	1862.7910	0.278	−325 to +50	6653.82	2.5720	0.19	0.01	...

TABLE 3—*Continued*

Ion	λ_{lab}[a] (Å)	f[a]	Δv[b] (km s^{-1})	λ_{obs}[c] (Å)	z_{abs}[d]	W_0[e] (Å)	σ[f] (Å)	Comments
High-Ionization Species: Redshifted Components								
Si III	1206.500	1.63	+300 to +500	4317.79	2.5788	0.42	0.02	Upper limit
N V	1238.821	0.1560	+150 to +600	4432.62	2.5781	0.42	0.01	...
N V	1242.804	0.07770	+150 to +600	4447.17	2.5783	0.28	0.01	...
Si IV	1393.7602	0.513	+150 to +600	4987.55	2.5785	0.59	0.02	...
Si IV	1402.7729	0.254	+150 to +600	5019.95	2.5786	0.32	0.02	...
C IV	1548.204	0.1899	+150 to +600	5539.54	2.5780	1.36	0.00	Upper limit, blended with C IV λ1550
C IV	1550.781	0.09475	+150 to +600	5549.17	2.5783	0.87	0.00	...
Al III	1854.7184	0.559	+300 to +500	6638.38	2.5792	0.06	0.01	...
Al III	1862.7910	0.278	+300 to +500	6666.32	2.5787	0.08	0.01	...
	...	...	...	...	...	...	...	...

NOTE.—The systematic errors are comparable to the random errors.
[a] Vacuum wavelengths and f-values from the compilation by Morton (2003) with recent updates by Jenkins & Tripp (2006).
[b] Velocity range, relative to $z_{sys} = 2.57393$, over which the equivalent widths were measured.
[c] Centroid wavelength of the absorption line in the observed frame.
[d] Measured absorption redshift.
[e] Rest-frame equivalent width.
[f] 1 σ random error for the rest-frame equivalent width.

infer the intensity of the radiation field responsible for heating the gas. In PDLAs this line is of particular interest as a means of gauging the contribution of the QSO to the radiation field impinging on the DLA, and thereby obtaining an indication of their physical separation.

We begin by working out the spontaneous [C II] 158 μm emission rate per hydrogen atom,

$$l_c = \frac{N(\mathrm{C\ II^*})}{N(\mathrm{H\ I})} h\nu_{ul} A_{ul} = \frac{N(\mathrm{C\ II^*})}{N(\mathrm{H\ I})} 3.0 \times 10^{-20}\ \mathrm{erg\ s^{-1}\ H\ atom^{-1}}, \quad (7)$$

where $h\nu_{ul}$ is the energy of a 158 μm photon and A_{ul} is the Einstein coefficient for spontaneous photon decay. From our VPFIT analysis,[17] we deduce $N(\mathrm{C\ II^*}) = 1.33 \times 10^{14}$ cm^{-2}; combining this value with $N(\mathrm{H\ I}) = 9.5 \times 10^{20}$ cm^{-2} (§ 3.2), we deduce from equation (7)

$$\log\left(l_c/\mathrm{erg\ s^{-1}\ H\ atom^{-1}}\right) = -26.38. \quad (8)$$

This value is not dissimilar to those measured in some intervening DLAs. Figure 13 shows the most recent compilation by Wolfe et al. (2005) of values of l_c measured in DLAs. While in about half the cases $\log l_c \lesssim -27$, values as high as that deduced here for the PDLA in Q2343–BX415 have been reported in a few cases.

Wolfe et al. (2003) developed the radiation transfer formalism required to interpret the values of l_c in terms of J_ν, the far-UV radiation intensity responsible for the heating rate of the gas. The main conclusion of their analysis, also discussed by Wolfe et al. (2005), is that while the DLAs where C II* λ1335.7 is undetected (the upper limits in Fig. 13) are consistent with the value of J_ν due to the integrated extragalactic background, $J_\nu^{tot} = J_\nu^{bg}$, those with higher values of l_c require an additional contribution ΔJ_ν, so that $J_\nu^{tot} = J_\nu^{bg} + \Delta J_\nu$. Wolfe et al. (2003) identify this additional

[17] Note that we did not constrain the redshift and Doppler parameter of the C II* gas with those values given in Table 4 due to the different excitation levels of the gas; VPFIT fitted a single component at $z = 2.57188$ with $b = 23.0$ km s^{-1}.

TABLE 4
ABSORPTION COMPONENTS OF LOW ION TRANSITIONS

Component	z_{abs}	Δv[a] (km s^{-1})	b (km s^{-1})	Fraction[b]
C1	2.57200	−162	41.6	0.96
C2	2.57351	−35	14.4	0.03
C3	2.57877	+406	26.6	0.01

[a] Velocity difference from $z_{sys} = 2.57393$.
[b] Fraction of the total column density of Si II.

TABLE 5
COLUMN DENSITIES FOR LOW-IONIZATION SPECIES

Ion	log$N$(C1) (cm^{-2})	log$N$(C2) (cm^{-2})	log$N$(C3) (cm^{-2})	log[N(C1) + N(C2)] (cm^{-2})
C II	>16.336	>14.836	14.421	>16.350
N I	14.987	13.463	13.810	15.000
O I	>16.890	>14.659	...	>16.893
Mg II	15.486	13.986	13.361	15.500
Al II	>14.546	>13.315	12.268	>14.571
Si II	15.783	14.234	13.778	15.795
P II	<13.686	<12.200	...	<13.700[a]
S II	15.380	...	...	15.380
Ti II	<12.585	...	...	<12.585
Cr II	13.577	...	...	13.577
Mn II	13.041	...	...	13.041
Fe II	15.229	13.744	12.599	15.243
Ni II	14.078	...	...	14.078
Zn II	12.898	...	...	12.898

NOTES.—The table presents the ion column densities measured for the three absorption components listed in Table 4. We attempted to fit all three components for each ion; in practice, for species which have only weak lines (e.g., S II and Zn II), C2 could not be distinguished from C1, so that a single component was fitted. In these cases, the weaker third component, C3, was not detected. We were also unable to fit C3 in O I, due to the blending of the O I λ1302 line with the main component of Si II λ1304. For reasons explained in the text, this third component was not used in our element abundance analysis. Instead we used the summed column density of the other two components, as given in the final column of the table.
[a] As P II λ1152 was blended with a Lyα line, we derived upper limits to the column densities of C1 and C2 under the assumption that their ratio is similar to that for Fe II.

TABLE 6
ELEMENT ABUNDANCES

Ion	log N (cm^{-2})	log (X/H)	log (X/H)$_\odot$[a]	[X/H]$_{PDLA}$[b]
H I	20.98	...	...	...
C II.....	>16.35	>−4.63	−3.61	>−1.02
N I	15.00	−5.98	−4.17	−1.81 ± 0.04
O I	>16.89	>−4.08	−3.31	>−0.77
Mg II.....	15.50	−5.48	−4.45	−1.03 ± 0.25:
Al II	>14.57	>−6.41	−5.54	>−0.87
Si II.....	15.79	−5.18	−4.46	−0.72 ± 0.04
P II.....	≤13.70	≤−7.28	−6.54	≤−0.74
S II.....	15.38	−5.60	−4.81	−0.79 ± 0.03
Ti II.....	≤12.59	≤−8.39	−7.08	≤−1.31
Cr II	13.58	−7.40	−6.35	−1.05 ± 0.04
Mn II.....	13.04	−7.94	−6.50	−1.44 ± 0.04
Fe II	15.24	−5.73	−4.53	−1.20 ± 0.02
Ni II	14.08	−6.90	−5.78	−1.12 ± 0.03
Zn II.....	12.90	−8.08	−7.37	−0.71 ± 0.06

NOTES.—The H I column density was measured by fitting the damping wings of the Lyα absorption line (see § 3.2). Column densities for all the other ions were determined from Voigt profile fitting with VPFIT (see Table 5).

[a] Solar abundance scale from Lodders (2003).

[b] $[X/H]_{PDLA} = \log(X/H) - \log(X/H)_\odot$. The errors quoted are from the VPFIT error estimates associated with each value of log N(X) and do not include the uncertainty in the determination of log N(H). The latter would result in the same offset for all elements.

component ΔJ_ν as the UV radiation from young stars within the galaxies hosting the DLAs and use this method to estimate the star formation rate of such systems.

We can follow the same line of reasoning and deduce the maximum contribution of Q2343–BX415 to the radiation field to which the PDLA is exposed, under the assumption of negligible contribution from in situ star formation. Comparison of the value of ΔJ_ν appropriate to the PDLA with the known luminosity of the quasar would then provide a lower limit to the distance between Q2343–BX415 and the PDLA—any local stellar contribution to ΔJ_ν would place the absorber further away from the quasar.

Applying the radiation transfer code of Wolfe et al. (2003)[18] with the parameters appropriate to the PDLA, redshift, metallicity, and dust-to-gas ratio (deduced from the observed [Fe/Zn] ratio, see § 5.2), we find that our measured log $l_c = -26.38$ implies $\Delta J_\nu = 2.0 \times 10^{-18}$ erg s^{-1} cm^{-2} Hz^{-1} sr^{-1} if the C II* absorption arises in a cold neutral medium (CNM), and $\Delta J_\nu = 4.4 \times 10^{-17}$ (in the same units) if it arises in a warm neutral medium (WNM). The former solution is the one generally adopted for DLAs (see Wolfe et al. [2003, 2005] for further details).

[18] The calculation was kindly performed for us by A. M. Wolfe.

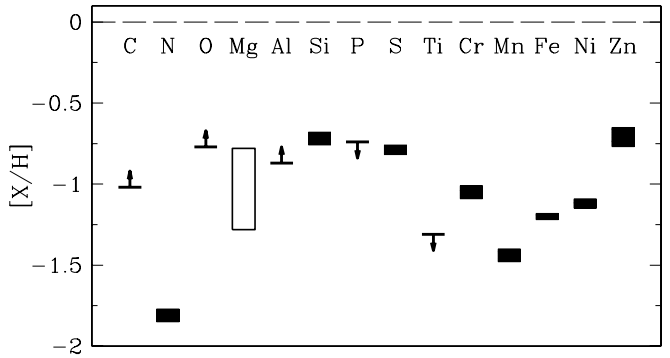

FIG. 6.—Element abundances of the PDLA in Q2343–BX415, relative to the solar abundance scale of Lodders (2003). Abundance determinations are shown by boxes, where the height of the box reflects the error estimate from VPFIT, while arrows indicate upper and lower limits. For reasons explained in the text, the measurement of the Mg abundance is uncertain, and is indicated here by an open box. [*See the electronic edition of the Journal for a color version of this figure*.]

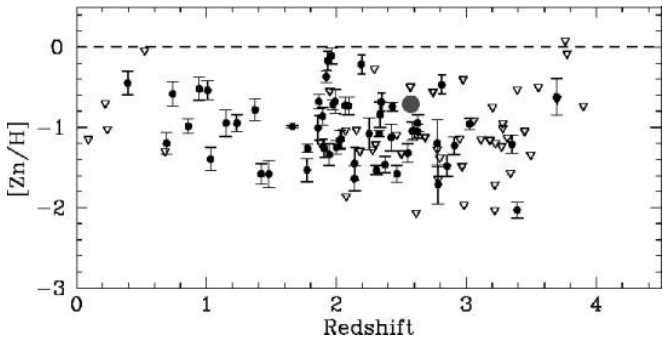

FIG. 7.—Metallicity of DLAs measured via the [Zn/H] ratio. The PDLA studied here is shown by the large circle; the other points are from the compilation of over 100 DLAs by Akerman et al. (2005). Filled circles are cases where the generally weak Zn II absorption lines have been detected, while open triangles are 3 σ upper limits corresponding to nondetections. [*See the electronic edition of the Journal for a color version of this figure*.]

These values of ΔJ_ν correspond to the excess over the Haardt & Madau (2001) extragalactic background at a wavelength of 1500 Å. The distance from Q2343–BX415 at which the QSO contributes this excess is then given by

$$d = \frac{1}{4\pi}\sqrt{\frac{L_\nu}{J_\nu}}, \tag{9}$$

where L_ν is the QSO luminosity at 1500 Å. We calculate this last quantity from the measured $G = 20.32$ broadband magnitude, extrapolating the QSO continuum to $\lambda_0 = 1500$ Å, and after small corrections to account for filter transmission curves, emission, and absorption lines. We find $L_{1500}^{Q2343-BX415} = 4.1 \times 10^{30}$ erg s^{-1} Hz^{-1} and therefore $d \geq 37$ kpc for the CNM solution. The WNM solution, if applicable, would lower the limit to $d \geq 8$ kpc.

9. DISCUSSION

The main results of the work presented in this paper are as follows.

1. We have obtained a high signal-to-noise ratio, medium-resolution, spectrum of the faint QSO Q2343–BX415 motivated by the presence of a strong DLA coincident in redshift with the

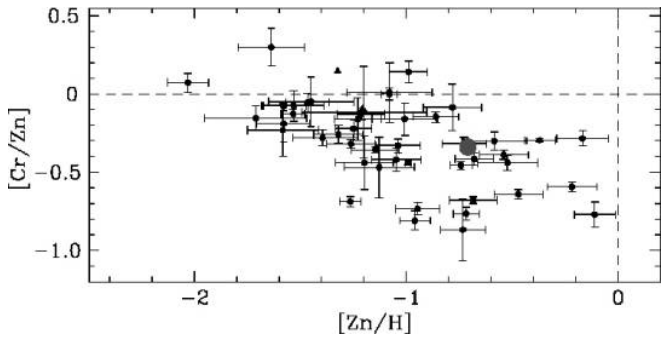

FIG. 8.—The dependence of the [Cr/Zn] ratio on metallicity in DLAs. The data are from Akerman et al. (2005), except for the large circle, which refers to the PDLA in Q2343–BX415. The [Cr/Zn] ratio gives an indication of the extent to which refractory elements are incorporated into dust grains. [*See the electronic edition of the Journal for a color version of this figure*.]

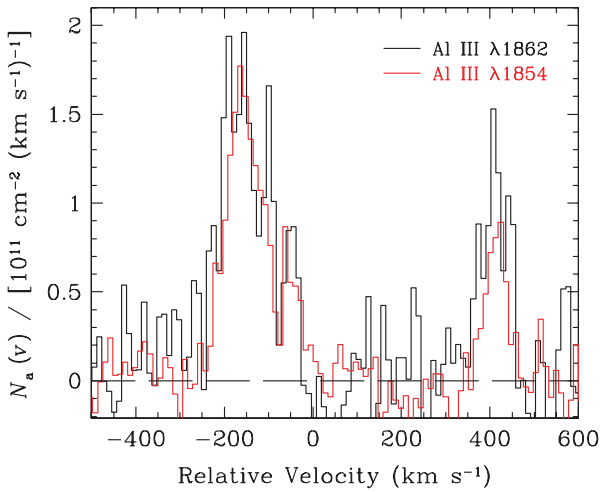

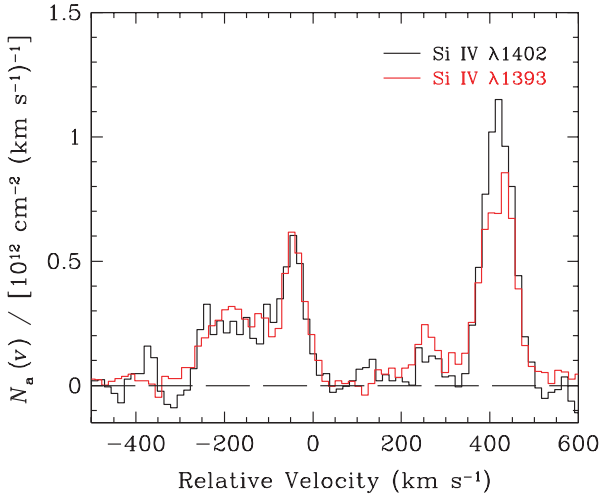

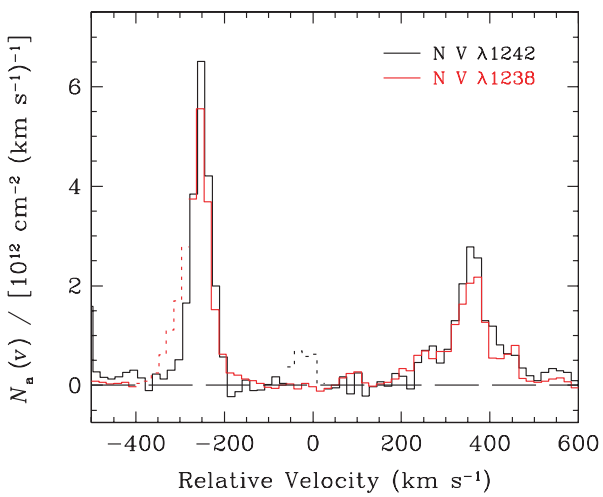

FIG. 9.—Apparent optical depth analysis of moderately and highly ionized species. Apparent column densities per unit velocity are displayed as a function of velocity (relative to $z_{sys} = 2.57393$); blending with lines from other species is flagged by a dotted line. The transitions shown in the legends are in increasing order of $f\lambda$ from the top. The higher values of $N_a(v)$ derived for the weaker, longer wavelength, members of the Al III, Si IV, and N V doublets in the redshifted component of the absorption are suggestive of partial coverage of the QSO continuum by the absorbing gas.

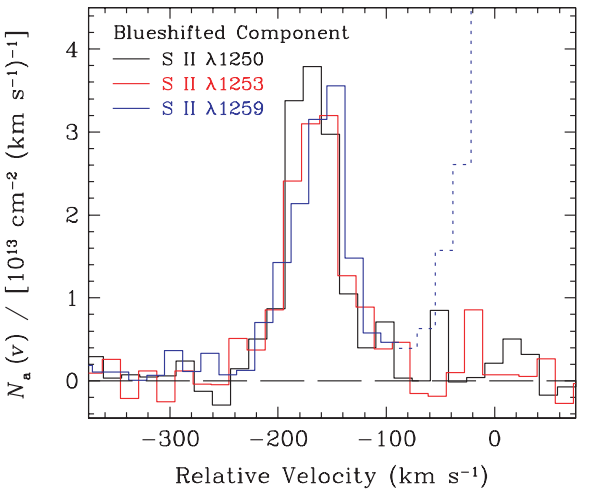

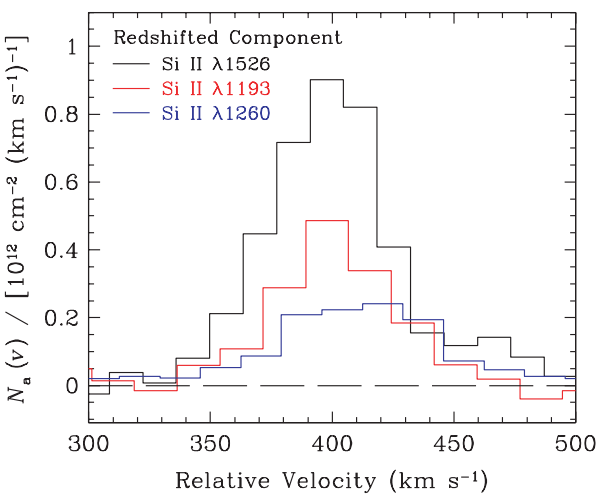

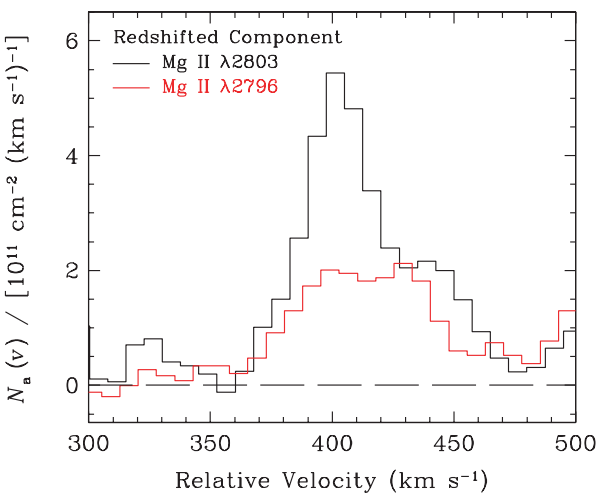

FIG. 10.—Apparent optical depth analysis of selected low ions. The transitions shown in the legends are in increasing order of $f\lambda$ from the top. The blueshifted absorption component is shown for the S II triplet (*top*), while the redshifted component is shown for three Si II lines (*middle*) and for the Mg II doublet (*bottom*). Blending with lines from other species is flagged by a dotted line.

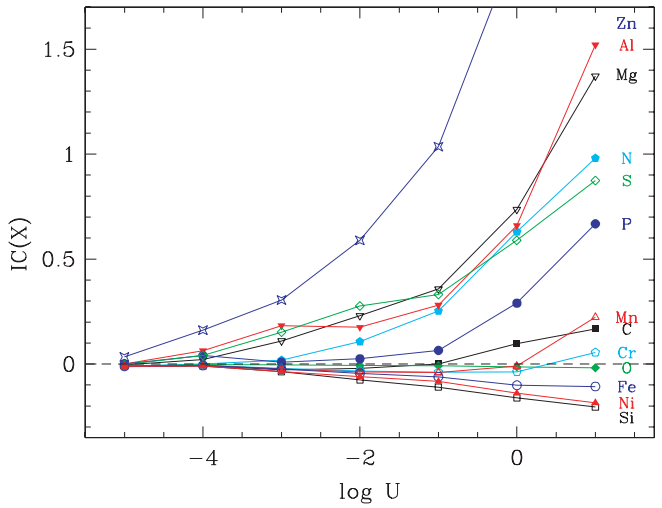

FIG. 11.—Logarithmic ionization corrections applicable to our abundance estimates in the PDLA (see eq. [5]), plotted as a function of the ionization parameter U, for a constant density model with $n(\mathrm{H}) = 10\ \mathrm{cm}^{-3}$. The corrections were computed using the photoionization code CLOUDY.

QSO. Our intention was to investigate gas in the vicinity of the quasar; in particular, if the DLA arises in the host galaxy of Q2343–BX415 it would allow a more comprehensive characterization of its chemical composition than is normally possible with other techniques that are based either on high-ionization absorption systems at $z_{\mathrm{abs}} \approx z_{\mathrm{em}}$ or on the analysis of emission lines from the AGN. Unlike previous studies of other proximate systems, we are aided by the precise knowledge of both absorption and emission redshifts, the former from metal lines in the DLA and the latter from narrow emission lines in the rest-frame optical and UV spectrum of Q2343–BX415.

2. We find that metal lines associated with the DLA consist of two sets of absorption components. One component is apparently moving toward the QSO, being redshifted by ~150–600 km s^{-1} relative to the systemic redshift $z_{\mathrm{sys}} = 2.57393$. This component is prominent in high-ionization lines and does not fully cover the continuum source, suggesting that it is physically close to the active nucleus of the galaxy. To our knowledge, this is the first time that gas falling onto the nucleus has been seen in absorption.

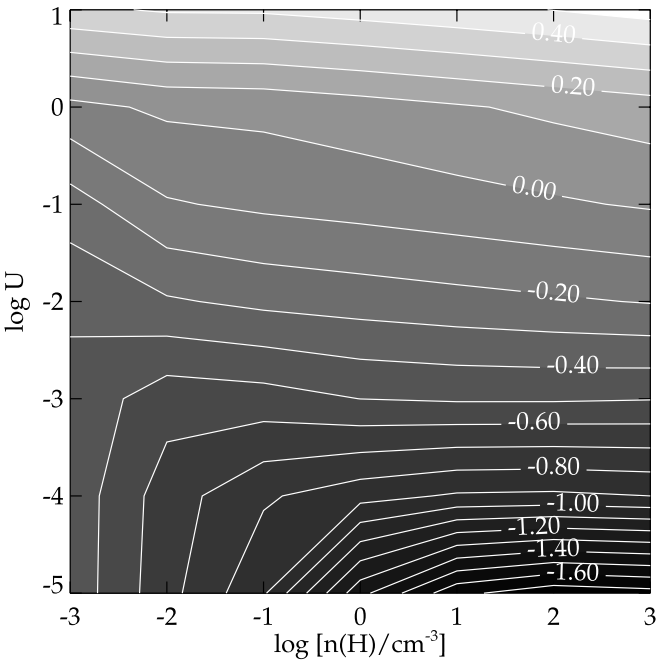

FIG. 12.—Values of log [N(Al III)/N(Al II)] computed by CLOUDY for a range of ionization parameters U and hydrogen densities n(H). [*See the electronic edition of the Journal for a color version of this figure.*]

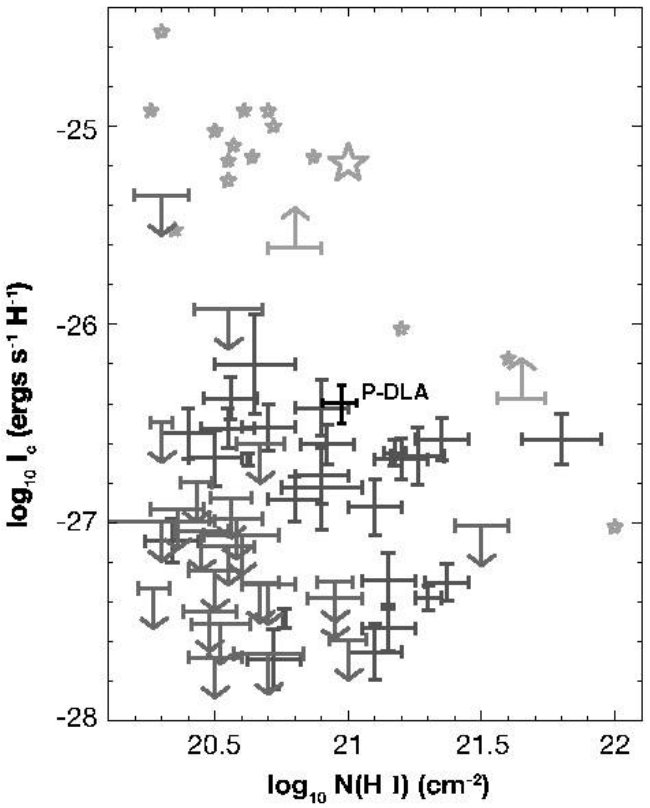

FIG. 13.—Compilation of available measurements of the [C II] 158 μm photon emission rate per H atom, l_c, in DLAs (adapted from Wolfe et al. 2005). Gray error bars are used for DLAs where N(C II*) has been measured, while downward arrows are 2 σ upper limits. Two lower limits (also 2 σ) are shown by upward arrows and the value deduced here for the PDLA in Q2343–BX415 is indicated by the black error bars. Small stars are values of l_c measured along different sight lines through the interstellar medium of the Milky Way; the large star is the value averaged over the disk of our Galaxy. The higher dust content of the Milky Way ISM is thought to be the main reason for the higher cooling (and heating) rates compared to most DLAs. [*See the electronic edition of the Journal for a color version of this figure.*]

3. The second set of absorption components is blueshifted, with velocities ranging from +50 km s^{-1} to −325 km s^{-1} relative to z_{sys}; the neutral gas has maximum optical depth in a component at $v = -162$ km s^{-1}. These velocities are of the same order of magnitude as those often encountered within star-forming galaxies at $z = 2$–3; in particular the shift of −162 km s^{-1} of the bulk of the neutral gas is the same as the mean offset between UV absorption lines and Hα emission measured in nearly 100 BX galaxies at $z \simeq 2.0$–2.6 by C. C. Steidel et al. (2008, in preparation). Such velocity offsets are normally interpreted as evidence for galactic-scale outflows in star-forming galaxies, suggesting that in the PDLA we may be seeing the outflowing interstellar medium of the host galaxy of Q2343–BX415.

4. The blueshifted absorption includes gas over a wide range of ionization, from neutral species to C IV and N V. The latter in particular is indicative of a strong nonthermal ionizing source, presumably due to the combination of the close proximity of *two* QSOs: Q2343–BX415 and Q2343+1232, which is located

only ~690 kpc away from Q2343–BX415. However, the gas in the DLA itself appears to be shielded from the Lyman continuum radiation from the two QSOs and from the metagalactic background: the low N(Al III)/N(Al II) ratio is indicative of a low-ionization parameter for the neutral gas. This in turn implies that it is possible to deduce element abundances without significant corrections for unobserved ion stages.

5. The presence of C II* in the PDLA gives a measure of the UV radiation field longward of the Lyman continuum, under the assumption of equilibrium between the cooling rate via [C II] λ158 μm emission and photoelectric heating from grains. The value of J_{1500} we deduce, adopting the radiation transfer formalism of Wolfe et al. (2003), is ~50 to ~1000 times greater than the metagalactic radiation field of Haardt & Madau (2001) depending on the temperature of the gas. If Q2343–BX415 is the main source of this intense radiation field, the PDLA must be located only a few tens of kpc from the QSO, more specifically at ~8 or ~37 kpc depending on whether the C II* absorption arises in a CNM or a WNM.

6. On the other hand, in the compilation by Wolfe et al. (2005) there are other intervening DLAs where the rate of grain photoelectric heating is as high as that measured here. Those authors attribute the excess radiation (over the metagalactic background) to OB stars in the host galaxies of the DLAs; any such contribution would increase the inferred distance of the PDLA from Q2343–BX415. While this remains a possibility, we note that (1) a stellar ionizing spectrum would not account for the presence of strong N V in the blueshifted absorption, which would then have to arise in a physically distinct region from the DLA (see, for example, Fox et al. 2007); and (2) as discussed in the Appendix, our deep imaging and follow-up spectroscopy of the field of Q2343–BX415 has not yet produced a plausible galaxy candidate (other than the host galaxy of the QSO) for the PDLA.

7. The overall metallicity of the DLA and its detailed chemical composition in 14 elements of the periodic table are similar to those encountered in the normal DLA population. With a metallicity of ~1/5 solar, the PDLA is a factor of ~2–3 more chemically enriched than the median at its redshift, but there is no evidence of the supersolar metallicities that have been claimed for associated, high-ionization systems (e.g., Petitjean et al. 1994). No peculiarities were found in the pattern of relative abundances of the different elements sampled, most of the departures from solar relative abundances being compatible with depletions of refractory elements onto dust grains. Interestingly, there is a remarkable similarity, in both the degree of metal enrichment and the relative abundances, between this PDLA and the other well-studied PDLA to date, the $z_{\rm abs} = 2.8110$ system toward Q0528–2505 (Lu et al. 1996; Ledoux et al. 2006).[19]

However, the chemical data are not of clear diagnostic value regarding the origin of the PDLA. Its overall metallicity of ~1/5 solar is intermediate between the values typical of intervening DLAs ($\langle Z_{\rm DLA}\rangle \simeq 1/15\ Z_\odot$; Akerman et al. 2005) and of star-forming galaxies ($Z_{\rm LBG} \simeq \frac{1}{3}$–$1\ Z_\odot$; Erb et al. 2006; Pettini et al. 2001) at redshifts $z = 2$–3. Its detailed abundance pattern is consistent with either interpretation (Wolfe et al. 2005; Pettini et al. 2002b). The finding that the metallicity is a factor of ~2–3 lower than that of most of the BX galaxies studied by Erb et al. (2006) may be an indication that the host galaxy of Q2343–BX415, if that is what we are detecting, is intrinsically (i.e., when its nucleus is not in an active phase) fainter than the $\mathcal{R} = 25.5$ limit of the BX survey. Alternatively, there may well be metallicity gradients between the central, star-forming regions of UV-bright galaxies (to which the measures of Erb et al. 2006 refer) and outer regions where the interstellar medium is predominantly neutral. However, such an effect is not seen in MS 1512-cB58, the only galaxy at $z = 2$–3 where such a comparison has been made up to now (Pettini et al. 2002b; Rix et al. 2004).

In summary, our detailed observations of the rest-frame UV spectrum of Q2343–BX415 provide us with several clues as to the origin of the proximate DLA, but it is not yet possible to fit all of them into an entirely self-consistent interpretation. On the one hand, the PDLA could result from the chance alignment of a foreground galaxy and Q2343–BX415. When compared with the bulk of the DLA population, there is nothing particularly unusual in its kinematics, metal enrichment, abundance pattern, and low degree of ionization reflected in the low Al III/Al II ratio. The relatively strong C II* absorption could be due to in situ star formation. However, this picture requires *two* velocity matches to be coincidental: not only between the redshifts of the absorber and the quasar host, but also between the neutral gas in the DLA and the high ions—particularly N V—which in this picture would have to located in a separate region from the neutral interstellar medium of the DLA galaxy.

On the other hand, if the DLA is physically associated with Q2343–BX415, then our observations indicate that the gas is outflowing from the host galaxy of the quasar with velocities and other properties that are very much in line with those of the superwinds seen in most star-forming galaxies at comparable redshifts. The placement of the neutral gas at a few tens of kpc from the active nucleus (from the C II* analysis) is suggestive of a shell of swept-up interstellar material. Its relatively low metallicity (compared with those typically encountered in the star-forming regions of UV-bright galaxies) may be an indication that the host galaxy is fainter and of lower mass than most BX galaxies studied so far—and yet it still harbors an AGN. However, the low Al III/Al II ratio implies that the DLA must somehow be shielded from the ionizing radiation from the active nucleus.

Regardless of the uncertain origin of the PDLA itself, we have probably detected gas associated with the AGN in the (mostly ionized) redshifted components, which have less than 100% covering factor. While it would be very interesting to examine the metallicity of these intrinsic absorbers—and compare it to that of the emission line gas—both determinations would be much more model dependent than the straightforward measurement of DLA abundances on which we have focused in this paper.

In closing, while we have not been able to conclusively establish the origin of the PDLA, observations as detailed as the ones presented here still emphasize the importance of further studies of proximate DLAs as probes of the environments of quasars at early times. Comparison of their properties and physical conditions with those of the "field" population of DLAs will help us better understand the nature of DLAs at large, as well as adding to our knowledge of the galaxies, or groups of galaxies, that host AGNs. It is thus well worth targeting the fields of QSOs with known PDLAs with the combined efforts of deep galaxy surveys and high-resolution absorption line spectroscopy; the two techniques together have the potential to provide some of the most valuable empirical constraints on AGN-driven feedback at high redshift.

[19] For this comparison, recent revisions to the solar abundance scale and the *f*-values of relevant atomic transitions must be taken into consideration.

It is a pleasure to acknowledge illuminating discussions with Bob Carswell, Gary Ferland, and Paul Hewett, and valuable suggestions from the referee, which have improved this paper. We are indebted to Art Wolfe, who generously helped with the interpretation of the C II* absorption. Part of this work was carried out during visits by Sam Rix and Art Wolfe to the Institute of Astronomy, Cambridge, supported by the Institute's visitors' grant. S. Rix also acknowledges the support of a PPARC Postdoctoral Research Fellowship. We thank the staff of the Keck Observatory for their expert assistance with the ESI and NIRSPEC observations, and the Hawaiian people for the opportunity to observe from Mauna Kea. Without their hospitality, this work would not have been possible.

APPENDIX

INTERVENING ABSORPTION LINE SYSTEMS

In addition to the PDLA, we recognize 11 intervening absorption line systems in our ESI spectrum of Q2343–BX415, at $z_{\rm abs} < z_{\rm sys}$ (see Table 7). These systems range in redshift from $z_{\rm abs} = 1.2058$ to 2.4862, and are mostly high-ionization C IV systems, although we also have one Mg II system and a rich, mixed-ionization system at $z_{\rm abs} = 2.1735$ in which we identify 17 absorption lines. All the intervening absorption lines are labeled (S1–S11) in Figures 4*a*–4*g* and, like those in the PDLA, were fitted with VPFIT to deduce the values of column density listed in Table 7.

As explained in § 1, Q2343–BX415 was discovered during a survey for galaxies and faint AGNs in the field of the brighter QSO Q2343+1232. Details of the full survey, which covers $\sim$0.3 deg^2 on the sky in 13 different fields, are given in Adelberger et al. (2005); Figure 14 shows the locations of the two QSOs and of nearby galaxies with measured redshifts. Within a circle of radius 30″ centered on Q2343–BX415 (corresponding to a separation of 241 proper kpc at the redshift of the quasar), there are 11 galaxies brighter than $\mathcal{R} = 25.5$ that satisfy the BM and BX color criteria of Steidel et al. (2004)[20]; nine of these have spectroscopically confirmed redshifts and in all nine cases $z_{\rm gal} \leq z_{\rm QSO}$ (see Fig. 14). Similarly, there are 19 BM/BX candidates at projected distances between 30″ and 60″; 10 have been confirmed spectroscopically and eight are at redshifts $z_{\rm gal} \leq z_{\rm QSO}$.

With the survey data in hand, it may be possible to identify the galaxies producing the 11 intervening absorption systems in the spectrum of Q2343–BX415. In order to assess whether any of the 17 galaxies at redshifts less than or equal to that of the quasar are associated with any of the 11 intervening absorption systems, we need to establish: (1) the systemic redshift, $z_{\rm gal,sys}$, of candidate absorbing galaxies; and (2) the plausible redshift difference $\Delta z = \left| z_{\rm gal,sys} - z_{\rm QSO,abs} \right|$ between the systemic redshift of a galaxy and the absorption redshift of any absorption line system that would still allow us to plausibly associate the former with the latter.

Point (1) is less straightforward than it may appear at first sight. While the spectral features of the galaxies can be measured to within an accuracy of $\sim$50 km s^{-1}, more significant uncertainties in $z_{\rm gal,sys}$ arise due to the existence of significant velocity fields *within* star-forming galaxies at $z = 2$–3, as evidenced by the several hundred km s^{-1} difference in the redshifts measured from different spectral features, such as nebular emission lines, interstellar absorption lines, and Lyα emission (e.g., Erb et al. 2004). To account for such shifts, we adopted the following strategy: (i) for galaxies where the Hα emission line had been detected, we assumed that $z_{\rm sys} = z_{\rm H\alpha}$ with a typical measurement error of $\pm$60 km s^{-1}; (ii) for galaxies without $z_{\rm H\alpha}$ determinations, we estimated $z_{\rm sys}$ from the average velocity difference between the Hα emission line and the interstellar absorption lines, as measured in a sample of nearly 100 BX galaxies at $z \simeq 2.0$–2.6 (C. C. Steidel et al. 2008, in preparation): $\langle \Delta v_{\rm H\alpha - IS\ abs} \rangle = 164 \pm 130$ km s^{-1}.

Concerning point (2), we considered a redshift difference Δz corresponding to $\Delta v = \pm 300$ km s^{-1} sufficient to account for rotation and/or large-scale outflows in the galaxies. Combining points (1) and (2), we then calculated for each galaxy a redshift range

$$z_{\rm range} = z_{\rm sys} \pm \frac{(2\delta v + 300)}{c}\left(1 + z_{\rm sys}\right), \tag{A1}$$

over which it may produce absorption in the spectrum of Q2343–BX415, where δv is the 1 σ error affecting our determination of $z_{\rm gal,sys}$ (as discussed above).

The results of this exercise are summarized in Figure 15 and Table 8. In the last column of Table 8 we give our assessment of the likelihood that a galaxy is the absorber, on a scale from 1 (highest likelihood) to 3 (lowest likelihood). Rank 1 is for galaxies that satisfy two conditions: (1) they are located less than 200 (proper) kpc from the line of sight to the quasar; and (2) the redshift of the absorber is within the redshift range over which the galaxy could produce absorption, calculated as in equation (A1). Rank 2 is for galaxies at impact parameters $200 < D/{\rm kpc} < 500$ that also satisfy condition (2), while rank 3 is assigned to one case where $z_{\rm abs}$ is close to, but just outside (by $\sim$125 km s^{-1}), $z_{\rm range}$.

Out of the 10 intervening systems for which we could potentially find the absorbing galaxies,[21] three of them, S3, S4, and S5, each have one highly ranked galaxy counterpart which is presumably the absorber. There are galaxies further away from the line of sight to Q2343–BX415 whose $z_{\rm range}$ also includes $z_{\rm abs}$ of S4 and S5; in the case of S4 one of them may be contributing to the absorption, as the line profiles show more than one component in C IV (see Fig. 4*b*, *middle*). S8 has a low probability counterpart, while S2, S6, S7, S9, S10, and S11 do not have any cataloged galaxies at the right redshifts. This could be due to the incompleteness of our photometric and spectroscopic catalogs, or maybe the galaxies responsible for these absorbers are fainter than $\mathcal{R} = 25.5$. Perhaps more surprising is the finding that there are four galaxies at impact parameters $D \lesssim 160$ kpc, Q2343–BX434, Q2343–BX417, Q2343–BX390, and Q2343–BX435, that apparently do not produce absorption lines even to the relatively high sensitivity limit of our ESI spectrum (corresponding to a 5 σ equivalent width limit $W_{1548} \simeq 50$ mÅ). However, on closer inspection of the spectrum, we find that certainly in two (and marginally in three) of these cases, the corresponding C IV absorption lines could be blended with other spectral features,

[20] As discussed by Adelberger et al. (2004) the BM/BX color criteria select galaxies in the redshift interval $z \simeq 1.5$–2.5.

[21] We discount here the Mg II system at $z_{\rm abs} = 1.2058$ (S1) because the BX/BM color criteria of Steidel et al. (2004) are inappropriate for finding galaxies at such a low redshift.

TABLE 7

Intervening Absorption Line Systems

λ_{obs}[a] (Å)	Identification	z_{abs}	Δv[b] (km s^{-1})	W_{obs}[c] (Å)	σ_{obs} (Å)	W_0[d] (Å)	σ_0 (Å)	log N[e] (cm^{-2})	Comments
				System S1: $\langle z_{abs} \rangle$ = 1.2058					
6168.19.....	Mg II 2796.3543	1.2058	−90 to 75	0.52	0.03	0.24	0.01	12.82 ± 0.04	...
6183.93.....	Mg II 2803.5315	1.2058	−90 to 75	0.32	0.03	0.14	0.01	12.82 ± 0.04	...
				System S2: $\langle z_{abs} \rangle$ = 1.7876					
4315.83.....	C IV 1548.204	1.7876	−75 to 75	0.89	0.04	0.32	0.02	14.27 ± 0.12	Slightly blended on redward side
4322.85.....	C IV 1550.781	1.7875	−75 to 75	0.62	0.06	0.22	0.02	14.27 ± 0.12	...
				System S3: $\langle z_{abs} \rangle$ = 2.0138					
4200.82.....	Si IV 1393.7602	2.0140	−75 to 75	0.24	0.06	0.08	0.02	13.03 ± 0.16	...
4227.58.....	Si IV 1402.7729	2.0137	−75 to 75	0.15	0.06	0.05	0.02	13.03 ± 0.16	...
4665.94.....	C IV 1548.204	2.0138	−75 to 75	0.57	0.04	0.19	0.01	13.77 ± 0.06	...
4673.76.....	C IV 1550.781	2.0138	−75 to 75	0.30	0.04	0.10	0.01	13.77 ± 0.06	...
				System S4: $\langle z_{abs} \rangle$ = 2.1735					
4423.51.....	Si IV 1393.7602	2.1738	−90 to 135	1.48	0.02	0.46	0.01	13.82 ± 0.08[f]	Upper limit, blended with N V λ1238
4451.76.....	Si IV 1402.7729	2.1735	−90 to 135	0.49	0.03	0.15	0.01	13.82 ± 0.08[f]	...
4844.61.....	Si II 1526.7070	2.1732	−90 to 135	0.36	0.05	0.11	0.02	14.87 ± 0.20	...
4913.56.....	C IV 1548.204	2.1737	−90 to 135	1.09	0.06	0.34	0.02	14.48 ± 0.14[f]	...
4921.61.....	C IV 1550.781	2.1736	−90 to 135	0.95	0.06	0.30	0.02	14.48 ± 0.14[f]	...
5104.44.....	Fe II 1608.4511	2.1735	−90 to 135	0.11	0.04	0.03	0.01	13.44 ± 0.09	...
5301.81.....	Al II 1670.7886	2.1732	−90 to 135	0.30	0.05	0.10	0.02	13.66 ± 0.54	...
5738.01.....	Si II 1808.0129	2.1737	−90 to 135	0.13	0.03	0.04	0.01	14.87 ± 0.20	...
5885.67.....	Al III 1854.7184	2.1733	−90 to 135	0.20	0.05	0.06	0.01	13.17 ± 0.19	...
5911.60.....	Al III 1862.7910	2.1735	−90 to 135	0.17	0.04	0.05	0.01	13.17 ± 0.19	...
7439.05.....	Fe II 2344.2139	2.1734	−90 to 135	0.36	0.05	0.11	0.02	13.44 ± 0.09	...
7535.89.....	Fe II 2374.4612	2.1737	−90 to 135	0.10	0.04	0.03	0.01	13.44 ± 0.09	Noisy
7561.09.....	Fe II 2382.7652	2.1732	−90 to 135	0.33	0.04	0.10	0.01	13.44 ± 0.09	...
8206.77.....	Fe II 2586.6500	2.1727	−90 to 135	0.02	0.05	0.01	0.02	13.44 ± 0.09	Noisy; in telluric-corrected region
8250.78.....	Fe II 2600.1729	2.1732	−90 to 135	0.29	0.05	0.09	0.01	13.44 ± 0.09	In telluric-corrected region
8874.52.....	Mg II 2796.3543	2.1736	−90 to 135	1.09	0.03	0.34	0.01	...	Saturated
8897.26.....	Mg II 2803.5315	2.1736	−90 to 135	0.96	0.03	0.30	0.01	...	Saturated
				System S5: $\langle z_{abs} \rangle$ = 2.1866					
4441.42.....	Si IV 1393.7602	2.1866	−110 to 140	0.14	0.03	0.05	0.01	12.78 ± 0.103	...
.....	Si IV 1402.7729	...	−110 to 140	0.05	0.04	0.02	0.01	12.78 ± 0.103	Noisy
4933.43.....	C IV 1548.204	2.1865	−110 to 140	1.00	0.06	0.31	0.02	14.03 ± 0.049	...
4941.55.....	C IV 1550.781	2.1865	−110 to 140	0.53	0.06	0.17	0.02	14.03 ± 0.049	...
				System S6: $\langle z_{abs} \rangle$ = 2.3156					
4621.09.....	Si IV 1393.7602	2.3156	−60 to 60	0.25	0.05	0.07	0.02	12.97 ± 0.21	...
5133.30.....	C IV 1548.204	2.3156	−60 to 60	0.23	0.03	0.07	0.01	13.33 ± 0.09	...
5141.73.....	C IV 1550.781	2.3156	−60 to 60	0.11	0.03	0.03	0.01	13.33 ± 0.09	...
				System S7: $\langle z_{abs} \rangle$ = 2.3284					
4639.01.....	Si IV 1393.7602	2.3284	−75 to 85	0.33	0.05	0.10	0.02	13.04 ± 0.12	...
4668.31.....	Si IV 1402.7729	2.3279	−75 to 85	0.29	0.04	0.09	0.01	13.04 ± 0.12	Upper limit, blended with Si II λ1304
5153.13.....	C IV 1548.204	2.3285	−75 to 85	0.32	0.03	0.10	0.01	13.43 ± 0.07	...
5161.30.....	C IV 1550.781	2.3282	−75 to 85	0.16	0.03	0.05	0.01	13.43 ± 0.07	...
				System S8: $\langle z_{abs} \rangle$ = 2.3801					
5233.12.....	C IV 1548.204	2.3801	−75 to 75	0.94	0.03	0.28	0.01	14.45 ± 0.17	...
5241.89.....	C IV 1550.781	2.3802	−75 to 75	0.82	0.04	0.24	0.01	14.45 ± 0.17	...
				System S9: $\langle z_{abs} \rangle$ = 2.4376					
5321.91.....	C IV 1548.204	2.4375	−75 to 75	0.24	0.04	0.07	0.01	13.27 ± 0.21	...
5331.09.....	C IV 1550.781	2.4377	−75 to 75	0.05	0.04	0.02	0.01	13.27 ± 0.21	...

TABLE 7—*Continued*

λ_{obs}[a] (Å)	Identification	z_{abs}	Δv[b] (km s^{-1})	W_{obs}[c] (Å)	σ_{obs} (Å)	W_0[d] (Å)	σ_0 (Å)	log N[e] (cm^{-2})	Comments
			System S10: $\langle z_{abs} \rangle$ = 2.4649 (Uncertain)						
5364.61.....	C IV 1548.204	2.4651	−55 to 60	0.26	0.03	0.07	0.01	13.30 ± 0.10	Upper limit; blended with Ni II λ1502
5373.06.....	C IV 1550.781	2.4647	−55 to 60	0.08	0.03	0.02	0.01	13.30 ± 0.10	...
			System S11: $\langle z_{abs} \rangle$ = 2.4862						
4858.82.....	Si IV 1393.7602	2.4861	−50 to 50	0.23	0.03	0.07	0.01	13.16 ± 0.21	...
4890.39.....	Si IV 1402.7729	2.4862	−50 to 50	0.17	0.04	0.05	0.01	13.16 ± 0.21	...
5397.33.....	C IV 1548.204	2.4862	−50 to 50	0.32	0.03	0.09	0.01	13.73 ± 0.23	...
5406.37.....	C IV 1550.781	2.4862	−50 to 50	0.23	0.03	0.07	0.01	13.73 ± 0.23	...

NOTE.—The systematic errors are comparable to the random errors.
[a] Vacuum heliocentric wavelengths.
[b] Velocity range for the equivalent width measurements, relative to $\langle z_{abs} \rangle$ for each system.
[c] Observed-frame equivalent width and 1 σ random error.
[d] Rest-frame equivalent width and 1 σ random error.
[e] Ion column density and 1 σ error computed with VPFIT.
[f] Multiple components fitted with VPFIT at $z_{abs} = 2.1734$ and $z_{abs} = 2.1741$.

which would make it hard to recognize them, while for Q2343–BX435 we find a tentative detection of a weak C IV doublet at $z_{abs} = 2.1096$.

A final comment concerns the fact that our as yet incomplete spectroscopic survey has already identified four galaxies that are at redshifts close to that of Q2343–BX415; these galaxies are indicated by red squares in Figure 14. While their impact parameters are too large to associate any of them with the PDLA, they do attest to the fact that Q2343–BX415 is part of a large-scale structure that includes bright star-forming galaxies as well as the bright quasar Q2343+1232.

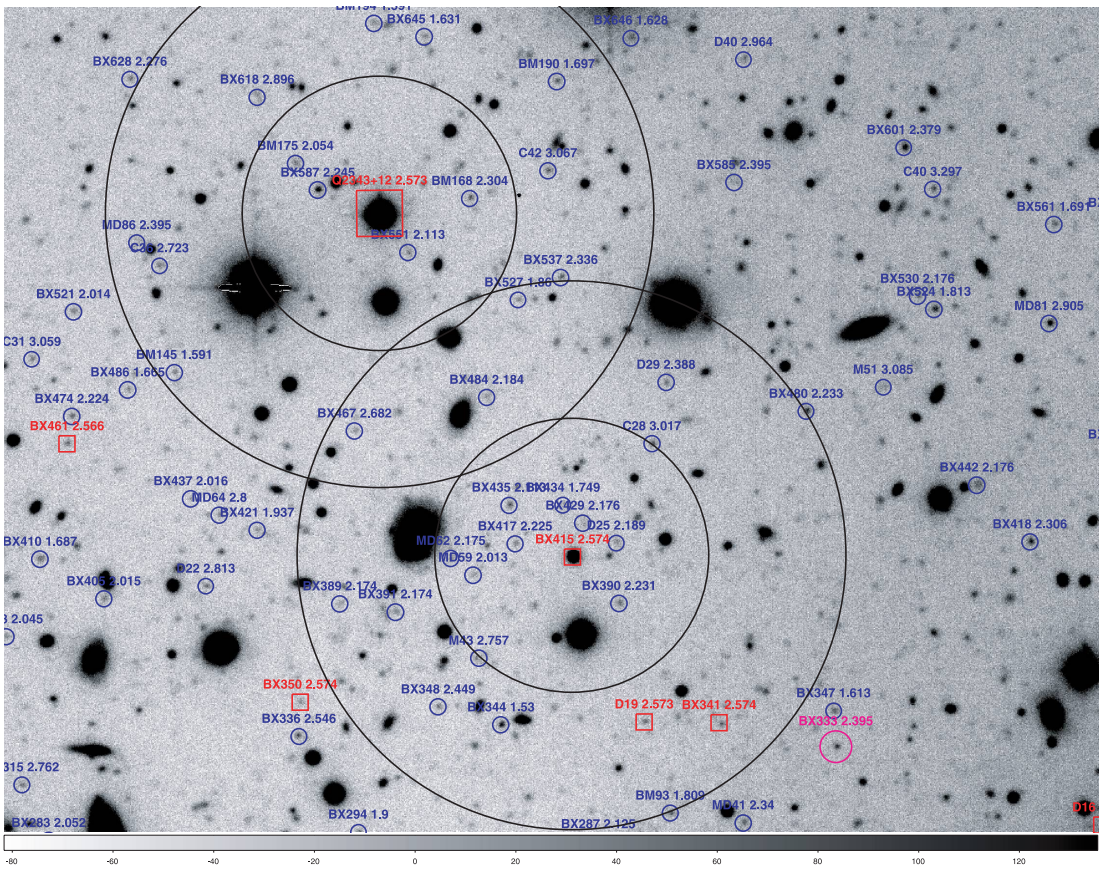

FIG. 14.—$\mathcal{R}$-band image of the field of the QSOs Q2343+1232 and Q2343–BX415, obtained with the prime focus camera of the 5.1 m Hale telescope at Palomar Observatory. The two QSOs are at the centers of concentric circles of radii 30″ and 60″. At the redshifts of the two quasars, $z_{sys} = 2.5727$ and 2.57393, respectively, the circles correspond to proper transverse distances of 241 and 481 kpc, respectively. Small blue circles indicate galaxies with spectroscopically confirmed redshifts; red squares are used to highlight galaxies at similar redshifts to Q2343+1232 and Q2343–BX415. The galaxy Q2343–BX333, highlighted with the magenta circle, shows AGN features.

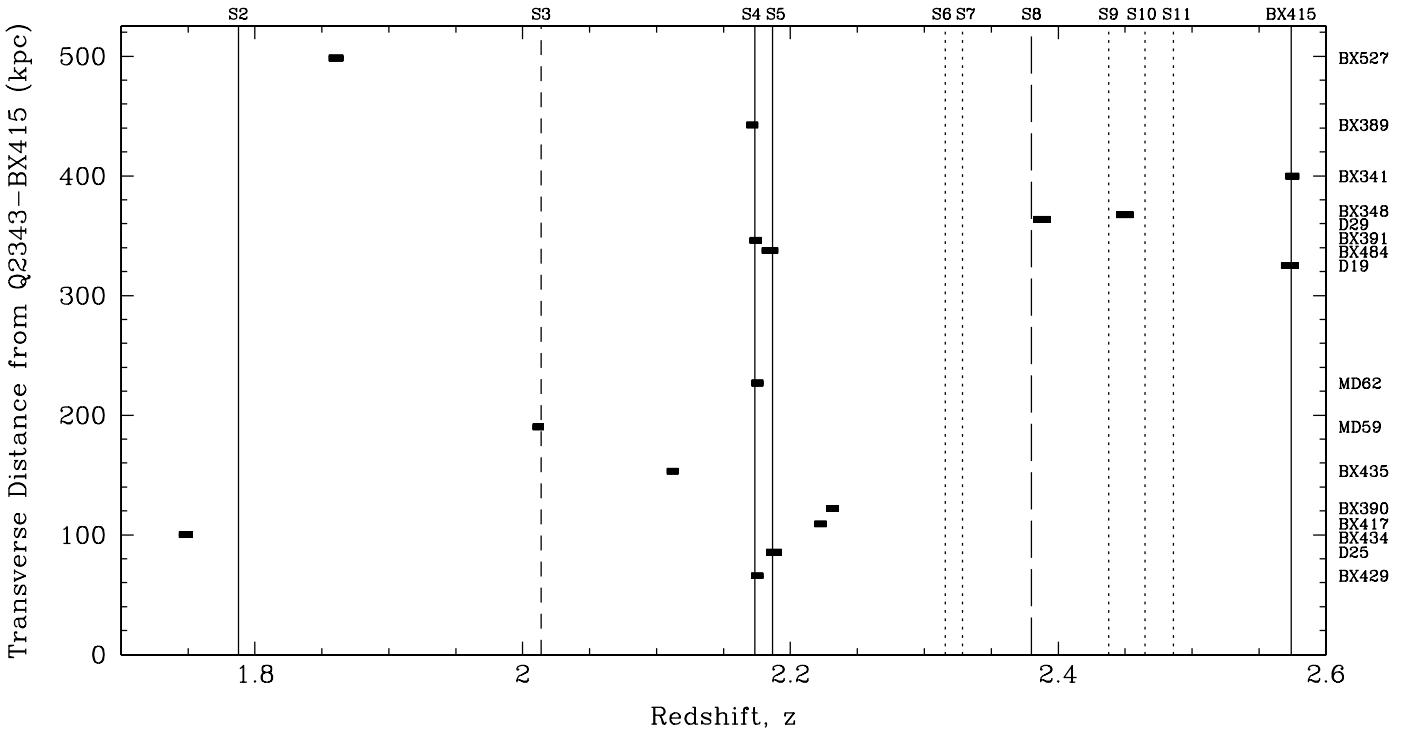

FIG. 15.—Comparison of the redshifts of 10 intervening absorption systems in line to Q2343–BX415 with those of 16 galaxies in the surrounding field. The absorption redshifts of the intervening systems are plotted with vertical lines; the line type gives an indication of the strength of the C IV absorption as follows: $W_{1548} > 0.3$ Å: *solid line*; 0.2 Å $< W_{1548} \leq 0.3$ Å: *long-dashed line*; 0.1 Å $< W_{1548} \leq 0.2$ Å: *short-dashed line*; $W_{1548} \leq 0.1$ Å: *dotted line*. The systemic redshift of Q2343–BX415 and its PDLA is also shown in a similar way. For comparison, galaxies with spectroscopic redshifts within $\sim 1'$ from Q2343–BX415 are represented by bars, where the width of each bar denotes the redshift range over which we estimate that these galaxies could produce intervening absorption systems (see the text for more details). The galaxies are identified in the right-hand margin of the panel. [*See the electronic edition of the Journal for a color version of this figure*.]

TABLE 8

CANDIDATE GALAXIES ASSOCIATED WITH THE INTERVENING ABSORPTION SYSTEMS

System ID	$\langle z_{\rm abs} \rangle$[a]	Candidate Galaxy IDs	$z_{\rm gal}$[b]	$\mathcal{R}$ (mag)	D[c] (kpc)	Rank[d]
S1	1.2058	...	...	...	...	...
S2	1.7876	...	...	...	...	...
S3	2.0138	Q2343–MD59	2.0116 ± 0.0042	24.99	190	1
S4	2.1735[e]	Q2343–BX429	2.1751 ± 0.0045	25.12	66	1
		Q2343–MD62	2.1752 ± 0.0045	25.29	227	2
		Q2343–BX391	2.1740 ± 0.0045	24.51	346	2
		Q2343–BX389	2.1716 ± 0.0044	24.85	443	2
S5	2.1866	Q2343–D25	2.1877 ± 0.0060	24.70	86	1
		Q2343–BX484	2.1847 ± 0.0060	24.77	338	2
S6	2.3156	...	...	...	...	...
S7	2.3284	...	...	...	...	...
S8	2.3801	Q2343–D29	2.3878 ± 0.0063	24.39	364	3
S9	2.4376	...	...	...	...	...
S10	2.4649	...	...	...	...	...
S11	2.4862	...	...	...	...	...

[a] Mean absorption redshift of the intervening system.

[b] Systemic redshift of the galaxy, and the range of redshifts over which we estimate that an associated absorbing system could arise (see text for more details).

[c] Impact parameter of candidate galaxy from the line of sight to Q2343–BX415.

[d] A ranking to indicate the likelihood of the galaxy being associated with the intervening system, where 1 is the highest and 3 the lowest (see text for details).

[e] Multiple components observed in this absorption system.

REFERENCES

Adelberger, K. L., Shapley, A. E., Steidel, C. C., Pettini, M., Erb, D. K., & Reddy, N. A. 2005, ApJ, 629, 636
Adelberger, K. L., Steidel, C. C., Shapley, A. E., Hunt, M. P., Erb, D. K., Reddy, N. A., & Pettini, M. 2004, ApJ, 607, 226
Akerman, C. J., Ellison, S. L., Pettini, M., & Steidel, C. C. 2005, A&A, 440, 499
Ellison, S. L., Yan, L., Hook, I. M., Pettini, M., Wall, J. V., & Shaver, P. 2002, A&A, 383, 91
Erb, D. K., Steidel, C. C., Shapley, A. E., Pettini, M., & Adelberger, K. L. 2004, ApJ, 612, 122
Erb, D. K., Steidel, C. C., Shapley, A. E., Pettini, M., Reddy, N. A., & Adelberger, K. L. 2006, ApJ, 647, 128
Espey, B. R., Carswell, R. F., Bailey, J. A., Smith, M. G., & Ward, M. J. 1989, ApJ, 342, 666
Ferland, G. J. 2000, in Rev. Mex. AA Conf. Ser., 9, 153
Ferland, G. J., Korista, K. T., Verner, D. A., Ferguson, J. W., Kingdon, J. B., & Verner, E. M. 1998, PASP, 110, 761
Foltz, C. B., Weymann, R. J., Peterson, B. M., Sun, L., Malkan, M. A., & Chaffee, F. H., Jr. 1986, ApJ, 307, 504
Fox, A. J., Petitjean, P., Ledoux, C., & Srianand, R. 2007, A&A, 465, 171
Gaskell, C. M. 1982, ApJ, 263, 79
Haardt, F., & Madau, P. 2001, in Clusters of Galaxies and the High Redshift Universe Observed in X-Ray, ed. D. M. Neumann & J. T. V. Tran (astro-ph/0106018)
Hamann, F., & Ferland, G. 1999, ARA&A, 37, 487
Howarth, I. D., Murray, J., Mills, D., & Berry, D. S. 2004, Starlink User Note 50.24 (Swindon: PPARC), http://www.starlink.rl.ac.uk/star/docs/sun50.htx/sun50.html
Howk, J. C., & Sembach, K. R. 1999, ApJ, 523, L141
Jenkins, E. B., & Tripp, T. M. 2006, ApJ, 637, 548
Ledoux, C., Petitjean, P., Fynbo, J. P. U., Møller, P., & Srianand, R. 2006, A&A, 457, 71
Lodders, K. 2003, ApJ, 591, 1220
Lu, L., Sargent, W. L. W., & Barlow, T. A. 1998, AJ, 115, 55
Lu, L., Sargent, W. L. W., Barlow, T. A., Churchill, C. W., & Vogt, S. S. 1996, ApJS, 107, 475
McLean, I. S., et al. 1998, Proc. SPIE 3354, 566
Moller, P., & Warren, S. J. 1993, A&A, 270, 43
Moller, P., Warren, S. J., & Fynbo, J. U. 1998, A&A, 330, 19
Morton, D. C. 2003, ApJS, 149, 205
Nagao, T., Maiolino, R., & Marconi, A. 2006, A&A, 447, 863
Oke, J. B. 1990, AJ, 99, 1621
Petitjean, P., Ledoux, C., Noterdaeme, P., & Srianand, R. 2006, A&A, 456, L9
Petitjean, P., Rauch, M., & Carswell, R. F. 1994, A&A, 291, 29
Pettini, M. 2007, in The Metal Rich Universe, ed. G. Israelian & G. Meynet (Cambridge: Cambridge Univ. Press), in press
Pettini, M., Ellison, S. L., Bergeron, J., & Petitjean, P. 2002a, A&A, 391, 21
Pettini, M., Ellison, S. L., Steidel, C. C., Shapley, A. E., & Bowen, D. V. 2000, ApJ, 532, 65
Pettini, M., Hunstead, R. W., King, D. L., & Smith, L. J. 1995, in Proc. ESO Workshop, QSO Absorption Lines, ed. G. Meylan (Berlin: Springer), 55
Pettini, M., Rix, S. A., Steidel, C. C., Adelberger, K. L., Hunt, M. P., & Shapley, A. E. 2002b, ApJ, 569, 742
Pettini, M., Shapley, A. E., Steidel, C. C., Cuby, J., Dickinson, M., Moorwood, A. F. M., Adelberger, K. L., & Giavalisco, M. 2001, ApJ, 554, 981
Prochaska, J. X., Hennawi, J. F., & Herbert-Fort, S. 2007, ApJ, submitted (astro-ph/0703594)
Prochaska, J. X., Howk, J. C., & Wolfe, A. M. 2003, Nature, 423, 57
Rix, S. A., Pettini, M., Leitherer, C., Bresolin, F., Kudritzki, R.-P., & Steidel, C. C. 2004, ApJ, 615, 98
Russell, D. M., Ellison, S. L., & Benn, C. R. 2006, MNRAS, 367, 412
Sargent, W. L. W., Boksenberg, A., & Steidel, C. C. 1988, ApJS, 68, 539
Sargent, W. L. W., Boksenberg, A., & Young, P. 1982, ApJ, 252, 54
Savage, B. D., & Sembach, K. R. 1991, ApJ, 379, 245
———. 1996, ARA&A, 34, 279
Sheinis, A. I., Bolte, M., Epps, H. W., Kibrick, R. I., Miller, J. S., Radovan, M. V., Bigelow, B. C., & Sutin, B. M. 2002, PASP, 114, 851
Steidel, C. C., Shapley, A. E., Pettini, M., Adelberger, K. L., Erb, D. K., Reddy, N. A., & Hunt, M. P. 2004, ApJ, 604, 534
Steigman, G., Strittmatter, P. A., & Williams, R. E. 1975, ApJ, 198, 575
Vanden Berk, D. E., et al. 2001, AJ, 122, 549
Vladilo, G., Centurión, M., Bonifacio, P., & Howk, J. C. 2001, ApJ, 557, 1007
Wolfe, A. M., Gawiser, E., & Prochaska, J. X. 2005, ARA&A, 43, 861
Wolfe, A. M., Prochaska, J. X., & Gawiser, E. 2003, ApJ, 593, 215